Computational epidemiology study of homeostatic compensation during sensorimotor aging

Niceto R Luque, Francisco Naveros, Denis Sheynikhovich, Eduardo Ros,
Angelo Arleo

HAL Id: hal-03500873

https://hal.sorbonne-universite.fr/hal-03500873v1

Submitted on 22 Dec 2021

Computational epidemiology study of homeostatic compensation during sensorimotor aging

Niceto R. Luque [a,b,*,1], Francisco Naveros [b,1], Denis Sheynikhovich [a], Eduardo Ros [b], Angelo Arleo [a]

[a] *Sorbonne Université, INSERM, CNRS, Institut de la Vision, 17 rue Moreau, F-75012 Paris, France*
[b] *Department of Computer Architecture and Technology, University of Granada (CITIC), Granada, Spain*

ARTICLE INFO

ABSTRACT

The vestibulo-ocular reflex (VOR) stabilizes vision during head motion. Age-related changes of vestibular neuroanatomical properties predict a linear decay of VOR function. Nonetheless, human epidemiological data show a stable VOR function across the life span. In this study, we model cerebellum-dependent VOR adaptation to relate structural and functional changes throughout aging. We consider three neurosynaptic factors that may codetermine VOR adaptation during aging: the electrical coupling of inferior olive neurons, the long-term spike timing-dependent plasticity at parallel fiber – Purkinje cell synapses and mossy fiber – medial vestibular nuclei synapses, and the intrinsic plasticity of Purkinje cell synapses Our cross-sectional aging analyses suggest that long-term plasticity acts as a global homeostatic mechanism that underpins the stable temporal profile of VOR function. The results also suggest that the intrinsic plasticity of Purkinje cell synapses operates as a local homeostatic mechanism that further sustains the VOR at older ages. Importantly, the computational epidemiology approach presented in this study allows discrepancies among human cross-sectional studies to be understood in terms of interindividual variability in older individuals. Finally, our longitudinal aging simulations show that the amount of residual fibers coding for the peak and trough of the VOR cycle constitutes a predictive hallmark of VOR trajectories over a lifetime.

1. Introduction

Healthy aging progressively degrades postural control and balance (Anson & Jeka, 2016; Brandt et al., 2005; Zalewski, 2015). The consequent loss of static and dynamic balance increases the risk of fall in older adults and hinders their autonomy (Desai et al., 2010; Piirtola & Era, 2006; Tinetti, 2003). Postural control is an adaptive process that relies on the integration of multimodal functions that concurrently mediate body and gaze stability (Mergner & Rosemeier, 1998). In this study, we focus on the vestibulo-ocular reflex (VOR), which ensures gaze stability during head motion (Grossman & Leigh, 1990) by generating rapid contralateral eye movements that stabilize images on the retinal fovea (Fig. 1A). The VOR plays a key role in maintaining balance, and VOR deficits can lead to oscillopsia (i.e., a perturbing illusory oscillation of the visual scene) during locomotion (Demer et al., 1994).

The neuroanatomical properties of the vestibular system degenerate with age (Allen et al., 2017; Anson & Jeka, 2016). The number of vestibular receptors (i.e., hair cells) decreases at a rate of about 6% per decade, tending to degenerate from middle age on, independently from pathology. The number of neurons in the vestibular nuclei undergoes a 3% loss per decade, starting at approximately 40 years of age (Alvarez et al., 2000; Lopez et al., 1996). Thus, fewer primary vestibular afferents reach the brain, in particular the downstream areas responsible for VOR adaptation such as the cerebellum (Allen et al., 2017). These structural vestibular losses would predict that aging impairs the detection and encoding of head motion, with a consequent decline of VOR function across the life span. Nevertheless, epidemiological studies report discordant patterns of results regarding VOR functional deficits during normal aging (Smith, 2016). Studies in the early 1990s showed age-dependent impairments of the rotatory VOR (r-VOR) (Baloh et al., 1993) in response to low-frequency (<1 Hz) sinusoidal rotations (Peterka et al., 1990) as well as to high-amplitude and high-velocity sinusoidal rotations (Paige, 1992). By contrast, recent studies reported that VOR gain (i.e., the ratio between the antagonist eye and head displacements) is preserved even in individuals aged 80 to 90 years. Li et al.

* Corresponding author at: Department of Computer Architecture and Technology, University of Granada (CITIC), Granada, Spain.
E-mail address: nluque@ugr.es (N.R. Luque).
[1] NL and FN share the first authorship.

(2015) conducted a cross-sectional VOR evaluation on a population of 110 healthy, community-dwelling individuals aged 26 to 92 years. They assessed VOR function with video head-impulse testing (vHIT), which provides a specific clinical assessment of the peripheral vestibular system. They reported that the r-VOR gain remains stable across participants aged up to approximately 80 years and it declines thereafter. McGarvie et al. (2015) measured the VOR gain by using the vHIT for all 6 semi-circular canals across a range of head velocities. They conducted a cross-sectional study on a population of 91 healthy, community-dwelling individuals aged 10 to 89 years (with about 10 subjects per decade). They reported that the r-VOR gain is unaffected by age, because it remain stable even in the group aged 80 to 89 years. Finally, Matiño-Soler et al. (2015) used the vHIT in the lateral semicircular canal plane to evaluate the r-VOR gain as a function of age and head velocity over a population of 212 healthy subjects. They observed a steady r-VOR until 90 years of age for low head impulse velocities and a decline thereafter. At higher-velocity head impulses, they reported a decrease of VOR gain in younger subjects (i.e., from 70 years onwards). Hence, although there are discrepancies in the results, these data consistently support the evidence that VOR function remains unaffected by age until 80–90 years, despite the structural degenerations that impair the vestibular system from middle age on.

Researchers have suggested that some compensatory processes may counter age-related vestibular losses, thus preserving the VOR in older adults (Jahn et al., 2003; Li et al., 2015; McGarvie et al., 2015). However, it is unknown what neural mechanisms are at stake in the brain to maintain VOR function and how they synergistically do so. In this study, we propose a model of cerebellum-dependent VOR adaptation to relate neuroanatomical and functional components of gaze stabilization during head rotations. The goal is to reproduce epidemiological data and to make testable predictions about the interplay of neuronal and plasticity mechanisms operating throughout aging. We hypothesize that three neurosynaptic factors are critical to understand how age affects the VOR:

(i) The first neurosynaptic factor is the electrical coupling between inferior olive (IO) neurons through gap junctions (Llinas et al., 1974; Sotelo et al., 1974), which determine the synchronicity and the oscillatory dynamics of the IO network (Lefler et al., 2020). We model the impact of aging on IO electrical coupling by considering the consequences of a degradation of GABAergic afferents from the medial vestibular nuclei (MVN) (Best & Regehr, 2009; Lefler et al., 2014). Because we assume that IO cells encode retinal slips during gaze stabilization (Ito, 2013; Luque et al., 2019; Naveros et al., 2019), we assess the consequences of age-related changes in IO electrical coupling on VOR function.

(ii) The second neurosynaptic factor is the long-term synaptic plasticity, both potentiation (LTP) and depression (LTD), that drives cerebellar adaptation (Badura et al., 2016; Clopath et al., 2014; Gao et al., 2012; Luque et al., 2019) and sensorimotor learning in general (D'Angelo et al., 2016). We explore the role of LTP and LTD as a *global* homeostatic compensatory process to enhance neural sensitivity during aging.

(iii) The third neurosynaptic factor is the intrinsic plasticity of Purkinje cell (PC) synapses (Jang et al., 2020; Shim et al., 2018), which modulates the excitability of PCs by adapting their membrane capacitance to morphological changes (Andersen et al., 2003; Zhang et al., 2010). We study the possible role of intrinsic plasticity of PC synapses as a *local* homeostatic process that operates during aging to compensate for the decreasing vestibular inputs as well as for the electro-responsiveness changes in PCs (Andersen et al., 2003; Zhang et al., 2010).

First, we examine the above neurosynaptic mechanisms independently of one another and we assess their individual impact on VOR adaptation as a function of age. Second, we simulate cross-sectional and longitudinal studies to explore how these mechanisms may codetermine the VOR temporal pattern observed throughout aging. Third, we attempt to identify the factors beneath the large interindividual variability of VOR performance during aging. We test the hypothesis that accounting for the variance in terms of adaptive compensation to residual fibers/connections can help explain the discrepancies between the epidemiological results reported in the literature concerning VOR function in individuals aged 80 to 90 years and thereafter.

2. Results

2.1. Cerebellum-dependent VOR adaptation

We framed VOR adaptation within a cerebellum-dependent forward control scheme (Lorente de Nó, 1933; Luque et al., 2019; Santina et al., 2001) (Fig. 1B). Computationally, the model reproduced the main properties of the cerebellar circuit and it consisted of five neural networks (Fig. 1C). A population of 100 mossy fibers (MFs) conveyed primary vestibular inputs (signaling head angular accelerations) onto the cerebellar network. MFs projected excitatory afferents onto 200 medial vestibular nuclei (MVN) and 2000 granule cells (GCs). GCs expanded the coding space of MFs inputs (Carrillo et al., 2018), and they transmitted the encoded sensory information to 200 Purkinje cells (PCs) through excitatory projections. An intrinsic plasticity mechanism regulated the excitability of model PCs (see Methods). PCs integrated the afferent signals from parallel fibers (PFs) (i.e., the axons of GCs), which elicited PC simple spikes (i.e., tonic firing mode). PCs also integrated the error-related signal from climbing fibers (CFs), i.e., inferior olive (IO) cells' axons. CFs elicited Purkinje complex spikes (i.e., bursting mode). PCs' responses (either simple or complex spiking) inhibited MVN cells. MVN cells also integrated inputs from MFs and IOs to generate the cerebellar output controlling eye movements (Fig. 1C). The CF-PC-MVN subcircuit comprised two symmetric microcomplexes that controlled leftward and rightward eye compensatory rotations, respectively (see Methods). Long-term plasticity (LTP and LTD) modulated PF–PC and MF–MVN synapses, whereas the remaining synaptic connections were either non-plastic or electrical, as among IO cells (Fig. 1C; see Methods).

We assessed cerebellum-dependent r-VOR adaptation using a 1 Hz sinusoidal head rotation protocol (i.e., in the natural head rotation range [0.05–5 Hz]; Leigh and Zee (2015). During 2500 s of simulation (Fig. 2), LTP and LTD plasticity shaped PF–PC and MF–MVN synaptic efficacies (which were randomly initialized) to adapt r-VOR gain and reduce retinal slips (i.e., the error sent by IO cells). After about 1000 s, r-VOR gain plateaued at 0.95 (Fig. 2A), a value consistent with experimental VOR data in humans during 1 Hz sinusoidal head rotations (Dits et al., 2013). As encoded by IO cell firing, retinal slip errors decreased from 8–9 Hz to 2–3 Hz as VOR accuracy improved (Fig. 2B). VOR learning was driven by a two time-scale cerebellar adaptation process: a fast adaptive phase mediated by plasticity at PF–PC cell synapses and a slow adaptive process mediated by plasticity at MF–MVN synapses (Supp. Fig. 1), in agreement with experimental data (Kassardjian et al., 2005; Shutoh et al., 2006).

2.2. Impact of age-related vestibular loss on the electrical coupling of IO neurons

The model IO neurons formed an electrically coupled network, whose recurrent dynamics were regulated by the PC-MVN-IO
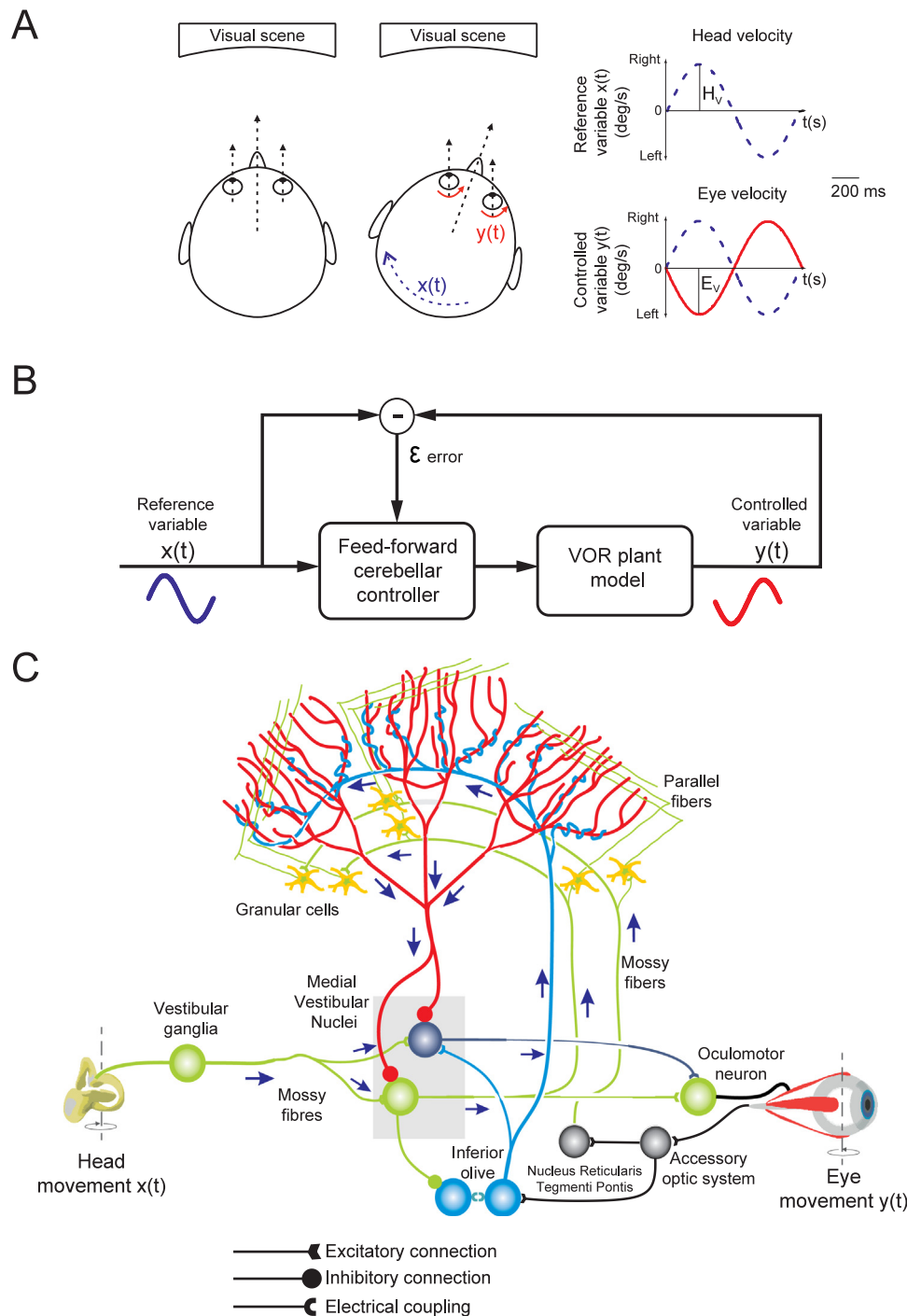
Fig. 1. Cerebellum-dependent adaptation of Vestibulo-Ocular Reflex (VOR). (A) Horizontal rotational VOR (i.e., r-VOR) stabilizes the visual field during horizontal head rotations, x(t), by producing contralateral eye movements, y(t). (B) Cerebellum-dependent VOR adaptation is modeled as a classic feedforward control loop. Cerebellar learning minimizes the error signal $\varepsilon(t)$, which is computed by comparing the input and output variables, i.e. x(t) and y(t), respectively. (C) Schematic representation of the main cerebellar layers, cells, and synaptic connections considered in the model. Mossy fibers (MFs) convey vestibular information onto granule cells (GCs) and medial vestibular nuclei (MVN). GCs, in turn, project onto Purkinje cells (PCs) through parallel fibers (PFs). PCs also receive excitatory inputs from the inferior olivary (IO) system. IO cells are electrically coupled and they deliver an error signal through the climbing fibers (CFs). MVN are inhibited by PCs and they provide the cerebellar output that drives oculomotor neurons. Spike-dependent plasticity occurs at PF–PC and MF–MVN synapses.

cerebellar loop (Fig. 1C). The inhibitory MVN action modulated the IO electrical coupling strength, which ultimately determined the synchronicity of IO firing (according to electrophysiological data: Best and Regehr (2009), Lefler et al. (2014) and Najac and Raman (2015)). A strong IO electrical coupling (i.e., a highly synchronized IO network) would allow large errors to be transmitted to PCs, enabling fast VOR learning, whereas a reduced IO electrical coupling would lead to slower but more accurate VOR adaptation (e.g., during late learning).

We sought to understand how the known progressive age-related decrease of the MVN GABAergic input to IO neurons (due to vestibular primary afferent loss) would affect IO network activity. We simulated two age groups (20 young subjects: 20 years old; 20 older subjects: 100 years old), and we linearly decreased the inhibitory MVN input to IO as a function of age (from a
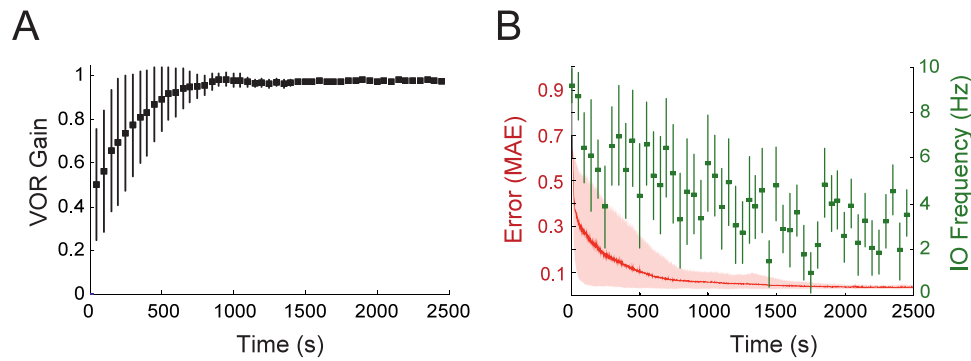
Fig. 2. Time course of VOR gain and error during cerebellar adaptation. (A) Evolution of the mean VOR gain during 2500 s of cerebellar learning under a 1-Hz sinusoidal vestibular stimulus (head horizontal rotation). The VOR was averaged across 40 individuals, with each individual obtained by a random initialization of weights at PF–PC and MF–MVN synapses. (B) Red curve: mean absolute VOR error during adaptation averaged over 40 individuals. Green squares: mean frequency of IO neurons throughout VOR adaptation.

maximum at 20 years to zero at 100 years; see Methods). We compared the dynamics of IO spatiotemporal firing patterns in a 5×5 lattice configuration, after that an error-related pulse activated the central IO neuron of the network (e.g., neuron 1 in Supp. Fig. 2A). The electrical coupling between IO neurons produced a rapid transient propagation within the network, eliciting a sequential bursting of IO cells along the lattice's outward radial direction (Supp. Figs. 2A, B). When comparing the IO network propagation patterns of the two age groups, we found that the central stimulation did elicit more rapid and pronounced membrane potential variations in the IO lattices of older individuals, which resulted in simpler on/off network dynamics as compared to young individuals (Fig. 3A and Supp. Fig. 2B). These transient on/off patterns produced a higher mean activation frequency in older IO networks (Fig. 3A). Also, the IO network's electrical coupling increased in the simulated aged individuals (Supp. Fig. 2C), in agreement with experimental data (Best & Regehr, 2009; Lefler et al., 2014; Najac & Raman, 2015).

We quantified the complexity of IO spatiotemporal patterns by using the Discrete Wavelet Transform (DWT) (Latorre et al., 2013). We considered these patterns as sequences of images (obtained every ms) and we estimated each image's compression by calculating the DWT coefficients. High (low) DWT values corresponded to complex (simple) spatial structures of IO network patterns at a given time. We found that the electrical coupling among IO neurons in older individuals led to significantly simpler spatiotemporal network activations, as compared to young individuals (Fig. 3B; ANOVA $F_{(294,16)} = 18$, $p < 10^{-7}$). This was consistent with a more uniform and synchronized activity of older IO neurons and a higher mean frequency (Fig. 3A). The simpler spatiotemporal dynamics of older IO networks were likely to induce a poorer capacity to encode retinal slips. We hence proceeded by testing the impact of this less effective error signaling on VOR performance.

2.3. Impact of age-related vestibular loss on r-VOR performance

We first investigated the consequences of age-related vestibular degradations on VOR function without any compensatory mechanism in the downstream cerebellar network. To do so, we blocked the intrinsic plasticity of PC synapses as well as LTP and LTD at MF–MVN and PF–PC synapses. We simulated a cross-sectional study over a large-scale study population of 2440 individuals aged 40–100 years, by taking a group of 40 individuals per each year of age (i.e., uniform distribution). Each individual underwent an independent 1 Hz head rotation protocol (during 2500 s, as above). The initial conditions (in terms of cerebellar synaptic weights) corresponded to those obtained after

r-VOR learning per each independent individual (Fig. 2A). Then, each of the 2440 individuals (independently) underwent a loss of randomly selected fibers and projections as a function of age, based on the following degeneration rates. We simulated a 3% loss of primary vestibular afferents per decade, which led to a loss of 0.3% MF–MVN connections per year, as well as 0.3% MF–GC projections per year (starting at 40 years). In addition, we simulated a loss of approximately 6% of GCs' axons per decade (according to Baloh et al. (1993), Bergström (1973), Renovell et al. (2001) and Viswasom et al. (2013), which engendered a degradation of 0.6% of PF–PC connections per year. The aging simulation results showed a steady decline of VOR function over lifetime, with the accuracy of r-VOR gain impaired in older individuals (Fig. 3C–E; −0.25%/year).

2.4. Cerebellar spike-timing dependent plasticity as a global homeostatic compensatory mechanism

We tested whether LTP and LTD at PF–PC and MF–MVN synapses could enhance the sensitivity of PCs and MVN to degraded inputs during aging. First, we analyzed the weight distributions at PF–PC and MF–MVN synapses after r-VOR learning as a function of age. We compared the synaptic weights of simulated young and older individuals (20 and 100 years, respectively). In both age groups, cerebellar learning led to antisymmetric weight distributions at both PF–PC and MF–MVN synapses (Fig. 4), corresponding to the two microcomplexes that controlled rightward and leftward eye movements. As expected, PCs' inhibitory action onto MVN generated opposite weight patterns at PF–PC compared to MF–MVN synapses (Fig. 4A, B vs. 4C, D). In older individuals, an increase of the remaining fibers' weights compensated for the loss of vestibular afferents (Fig. 4B, D). When comparing the distributions obtained by the normalized sums of synaptic weights across PFs (i.e., to estimate the input drive received by PCs), we found platykurtic-like distributions in older individuals (Fig. 4B, D) as compared to more leptokurtic profiles in young individuals (Fig. 4A, C). The ratio between the number of saturated synaptic weights and the number of active afferents increased with age: 28% in young vs. 64% in older PF–PC synapses (Fig. 4A vs. B); and 21% in young vs. 31% in older MF–MVN synapses (Fig. 4C vs. 4D). Consequently, the neural drive (defined as the area obtained by convolving a unitary impulse signal with the weight distributions) increased with age: it was 2.64 times larger in the older PF–PC synaptic distribution and 1.64 times larger in the older MF–MVN synaptic distribution, as compared to younger individuals, respectively.

We then ran a second cross-sectional aging simulation to test the role of LTP and LTD in preserving VOR in a population of
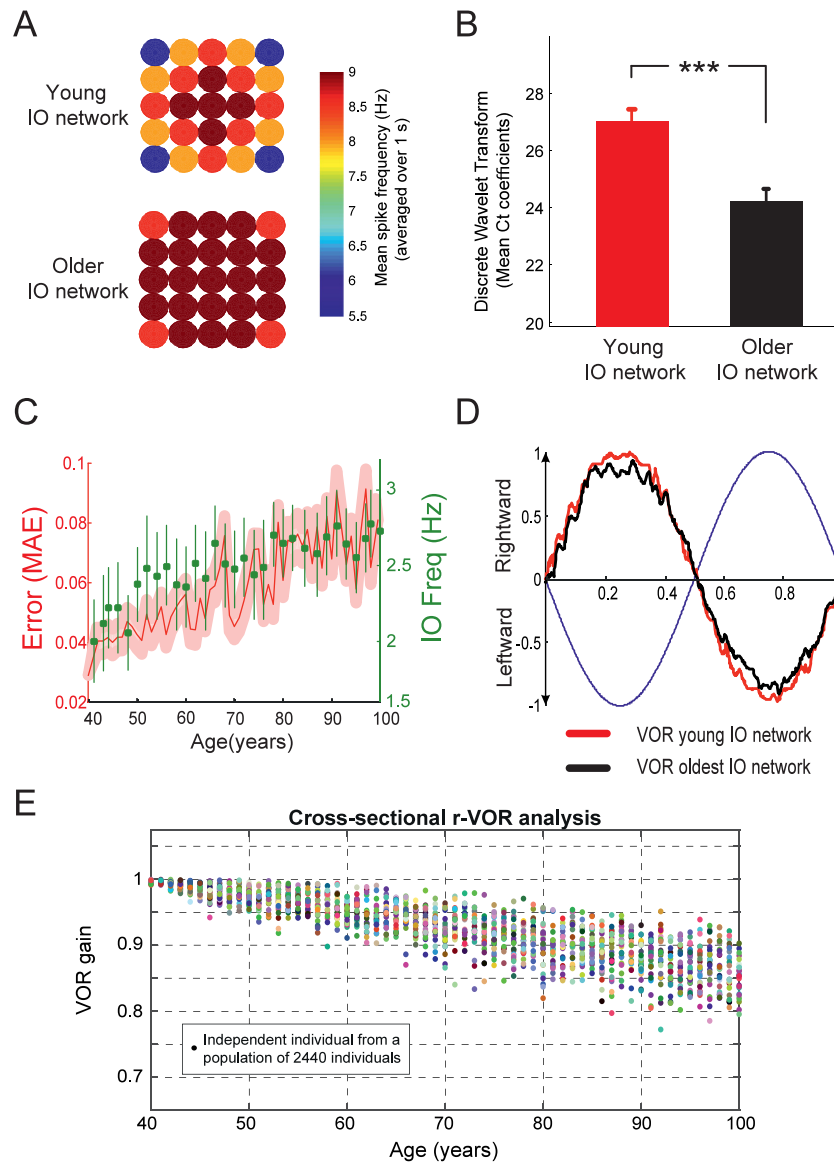
Fig. 3. Impact of age-related vestibular loss on IO electrical coupling and cerebellum-dependent VOR adaptation. (A) Mean frequency, averaged over 20 young (20 yo, top) and 20 older (100 yo, bottom) individuals, across a cluster of 5 × 5 IO cells (lattice configuration, Nobukawa and Nishimura (2016)) during the first second of VOR adaptation under a sinusoidal vestibular stimulus of 1 Hz. (B) Discrete Wavelet Transformation (DWT) applied to the snapshot sequence of the IO membrane potentials (Supp. Fig. 2 A) obtained during the first second of VOR adaptation for a young (20 yo) and an older (100 yo) individual. (C) Mean absolute VOR error (red curve) and corresponding mean IO frequency (green squares), in the presence of altered electrical coupling between IO neurons throughout aging. (D) Compensatory eye velocity function in the presence of young (red curve) and older (black curve) IO networks. (E) Cross-sectional simulation over a study population of 2440 individuals (each colored dot represents an individual) aged from 40 to 100 years (40 individuals per each year of age). Only the effect of age-related vestibular loss and IO coupling alteration was considered in this simulation, with no compensatory mechanism operating in the downstream cerebellar network. Each individual underwent an independent 1 Hz r-VOR protocol (during 2500 s). (For interpretation of the references to color in this figure legend, the reader is referred to the web version of this article.)

2440 individuals across a lifetime. We found that compensatory LTP and LTD at PF–PC synapses and MVN synapses preserved sensorimotor associations underpinning VOR until approximately 80 years of age (Fig. 4E). After that, we observed an increasing performance variance across individuals, and r-VOR gain declined in the group aged 85–100 years (−0.9%/year).

2.5. Intrinsic plasticity at PC synapses as a local homeostatic mechanism

The detailed PC model reproduced the three characteristic spiking patterns observed experimentally (Fig. 5A): simple spiking response (i.e., tonic firing at 10–250 Hz), complex spiking response (i.e., bursting activity up to 600 Hz), and post-complex spike pauses. We previously showed that PC spike burst-pause dynamics are likely to play a key role in VOR adaptation and reversal learning (Luque et al., 2019). Here, we investigated the consequences of age-dependent changes of PC excitability on VOR function. With aging, the number and the surface of PC synapses are known to decrease significantly (Zhang et al., 2010). The average synaptic size, however, exhibits a negative correlation to the synapse number during aging (Bertoni-Freddari et al., 1996, 1986; Chen & Hillman, 1999). This negative correlation helps maintain synaptic transmission between aging neurons thus indicating a compensatory mechanism of dendritic deafferentation (Monteiro et al., 1992). We reasoned that intrinsic plasticity could adjust PCs' response during aging, thus operating as a local homeostatic mechanism by adapting PC membrane capacity. The
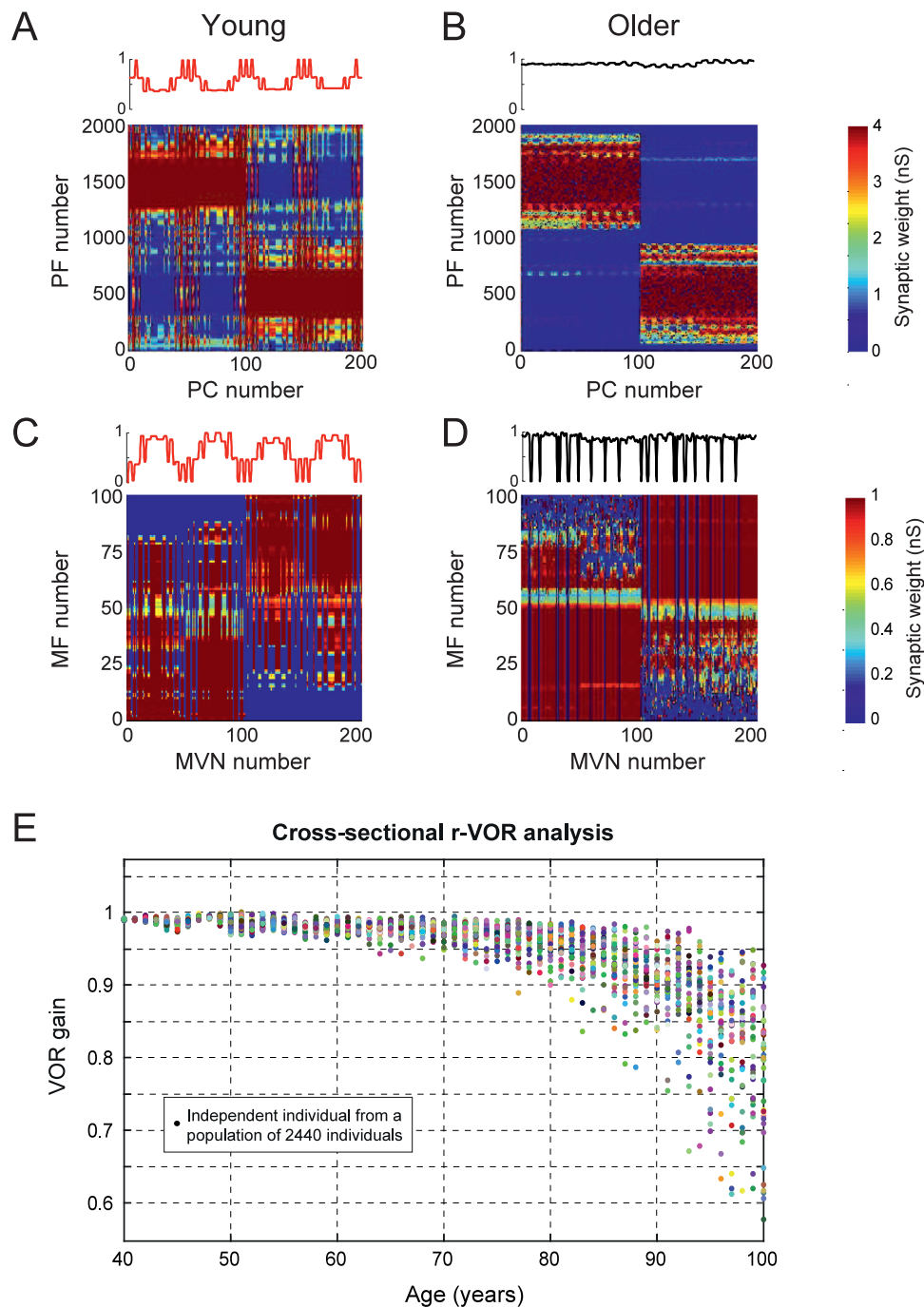
Fig. 4. Cerebellar LTP/LTD operates as a global homeostatic compensatory mechanism. (A, B) Synaptic weight distributions obtained at PF–PC connections by averaging over 20 young individuals (20 yo) and 20 older ones (100 yo). Each individual underwent an independent 1 Hz r-VOR adaptation (during 2500 s). The weights that correspond to the two cerebellar microcomplexes devoted to the control of rightward and leftward eye movements are visible. Top traces represent the normalized cumulative weight distribution along the PC axis. (C, D) Synaptic weight distributions at MF–MVN connections by averaging over 20 young individuals (20 yo) and 20 older ones (100 yo). The antisymmetric distributions with respect to (A, B) are caused by the inhibitory PC projections onto MVN. Top traces represent the normalized cumulative weight distribution along the MVN axis. (E) Cross-sectional aging simulation accounting for vestibular loss, IO electrical coupling alterations, and LTP/LTD at PF–PC and MF–MVN synapses. Each colored dot represents an individual from a population of 2440 individuals aged from 40 to 100 years (40 individuals per each year of age). (For interpretation of the references to color in this figure legend, the reader is referred to the web version of this article.)

membrane capacitance of modeled PCs decreased as a function of age (Fig. 5B; see Methods). This led to increased tonic firing rates in older PCs (Fig. 5C), consistent with electrophysiological data (Zhang et al., 2010). We also assessed the relationship between the duration of post-complex spike pauses and the duration of pre-complex spike ISIs (Inter Spike Intervals) in model PCs. We realized this measure by incrementally increasing PF inputs while maintaining the CF stimulation constant (i.e., only ISIs immediately following complex spikes were considered for this analysis, as in experimental data Grasselli et al. (2016). The PC model with the intrinsic plasticity mechanism predicted that the linear relation between the duration of post-complex spike pauses and the duration of pre-complex spike ISIs should be preserved during aging (Fig. 5D; $R^2 = 0.9932$; $p < 10^{-4}$).
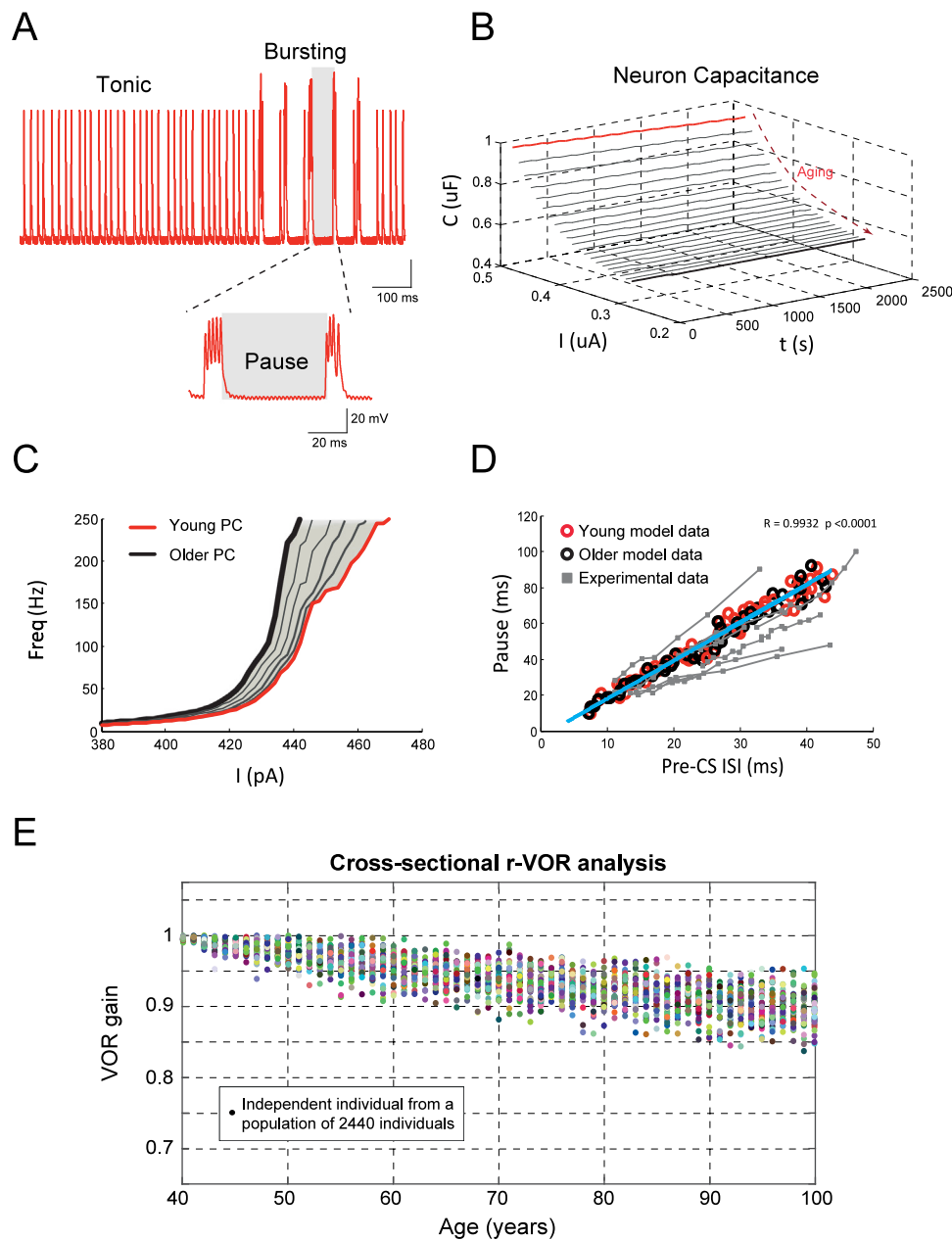
Fig. 5. Intrinsic plasticity of PC synapses acts as a local homeostatic mechanism. (A) Trimodal spiking patterns of modeled PCs: tonic firing, corresponding to simple spikes elicited by PF inputs; bursting mode, during which complex spikes (bursts of spikes) are elicited by CFs (Palay & Chan-Palay, 2012) (∼500 synapses) that can even suppress simple spiking; and silent mode, corresponding to an extended hyperpolarization period called 'post-complex spike pause'. (B) Modulation of the membrane capacitance of modeled PCs as a function of age by means of intrinsic plasticity. (C) Firing rate of PCs in young vs. older individuals measured with PCs operating in spiking tonic mode (10-250 Hz). (D) Correlation between pause duration and pre-complex spike ISI duration in modeled young and older PCs (red and black circles, respectively), as well as in real PCs (Grasselli et al., 2016) (gray squares). (E) Cross-sectional simulation over a study population of 2440 individuals (aged from 40 to 100 years, with 40 individuals per each year of age; each colored dot represents an individual) accounting for vestibular loss, IO electrical coupling chances, and intrinsic plasticity of PC synapses. (For interpretation of the references to color in this figure legend, the reader is referred to the web version of this article.)

We then ran a third aging simulation to test to what extent PC intrinsic plasticity may act when the vestibular loss occurred. Similar to the first cross-sectional simulation, we considered a population of 2440 individuals that underwent the same VOR adaptation protocol (1 Hz sinusoidal rotation during 2500 s). The same initial conditions and the same age-dependent structural degenerations were also simulated (see Section 2.3). LTP and LTD plasticity at MF–MVN and PF–PC synapses were blocked to isolate the effect of the local homeostatic mechanism provided by the intrinsic plasticity of PCs. We found that PCs' increasing excitability could only partially counterbalance the decreased depolarizing

currents elicited by PFs throughout aging. This resulted in a quasi-linear decrease of r-VOR gain across lifetime (−0.17%/year), along with an increasing interindividual variability (Fig. 5E).

2.6. Impact of aging on the VOR function: Full cross-sectional study

We then combined all age-related factors and compensatory mechanisms examined so far to assess their synergistic impact on r-VOR adaptation. We ran a fourth cross-sectional analysis on another cohort of 2440 individuals. LTP and LTD at MF–MVN and PF–PC synapses provided a global homeostatic adaptation, a
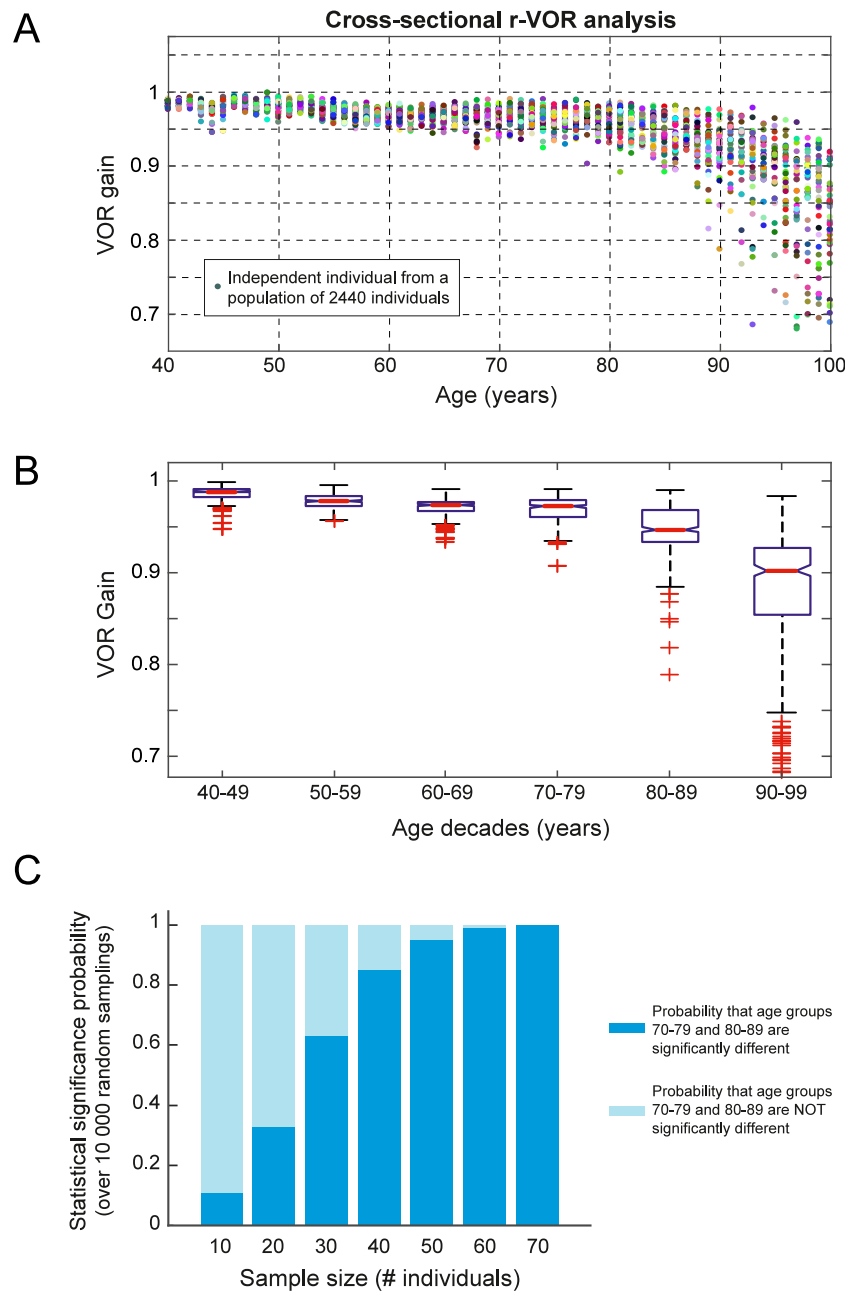
Fig. 6. Impact of aging on VOR: cross-sectional study. (A) Cross-sectional aging simulation accounting for vestibular loss, IO electrical coupling changes, PC intrinsic plasticity, and LTP/LTD at PF–PC and MF–MVN synapses. A study population of 2440 individuals (age range: 40–100 years; 40 individuals per each year of age; each colored dot represents an individual) underwent the same r-VOR protocol (1 Hz head rotation during 2500 s). (B) Comparison of r-VOR gain across decade age bands (with 400 individuals per decade). (C) Probability that r-VOR gain in age groups 70–79 and 80–89 is statistically different as a function of sampling size (computed over 10 000 random iterations per each sampling size). (For interpretation of the references to color in this figure legend, the reader is referred to the web version of this article.)

necessary condition for the model to adapt, whereas the intrinsic plasticity of PC synapses provided a complementary local homeostatic adaptation. The computational epidemiological results suggested that the considered neurosynaptic factors concurrently shaped r-VOR function across the life span. VOR gain remained unaffected by age until approximately 80–90 years (Fig. 6A). PCs' intrinsic plasticity further sustained VOR function compared to when only LTP and LTD were present (Fig. 4E,). The variability across individuals increased significantly after 90 years (Fig. 5), and VOR gain declined steadily thereafter (−0.8%/year). Local and global adaptation shaped the input drive of PCs and MVN neurons to compensate for afferent losses during lifetime (Supp. Fig. 3).

To compare our results against human cross-sectional data (Li et al., 2015; Matiño-Soler et al., 2015; McGarvie et al., 2015), we analyzed VOR gain changes across decade age bands (Fig. 6B). Each age band included 400 simulated individuals. A multiple comparison post hoc test showed that VOR function began to decline during the 80–89 age band, and it continued to decrease thereafter (ANOVA $F_{(7,3032)} = 736.2$, $p < 10^{-9}$). Then, given the large interindividual variability observed at older ages (Fig. 6A, B), we investigated to what extent the sample size may affect the outcome of multiple comparison analyses across age groups. We considered a set of different sample sizes: 10, 20, 30, etc. For each sample size (e.g., 10), we randomly sampled a corresponding number of individuals (e.g., 10) from the population of 400

individuals per each decade age band. Then, we ran a multiple comparison post hoc analysis across age groups. We repeated this process 10 000 times and we computed the overall probability of observing a statistically significant difference between VOR gains (Fig. 6C). This model-based analysis showed that a sample size of 50, or greater, individuals per decade would capture the statistical difference between the 70–79 and 80–89 age groups with a probability of 0.95. It also suggested the following: for a sample size of 10 individuals per decade (as in McGarvie et al., 2015), the probability of observing a significant r-VOR difference between 70–79 and 80–89 age groups would be as low as 0.11; for a sample size of 20 individuals per decade (as in Matiño-Soler et al., 2015), the predicted statistical significance probability would be as low as 0.33; and for a sample size equal to 30 individuals per decade (as in Li et al., 2015), the probability of observing a significant statistical difference would be equal to 0.63.

2.7. Impact of aging on the VOR function: Full longitudinal study

We ran a longitudinal aging simulation by combining all considered age-related factors and compensatory mechanisms. We took a study population of 40 individuals, and we simulated a 61-year follow-up for each individual (i.e., from 40 to 100 years). Again, initial conditions and structural degenerations over lifetime were simulated as in Section 2.3. However, in contrast to previous scenarios, these neural losses accumulated across each individual's lifetime. VOR performance across the study population remained unchanged by age until approximately 85–90 years, and it declined afterwards (Fig. 7A). The interindividual variability increased significantly during the last 15-year period (85–100 years), becoming approximately five times larger at 100 years as compared to 85 years (Supp. Fig. 4).

Finally, we investigated the underlying factors that determined the difference between steady and declining VOR trajectories in individuals aged 85–100 years (e.g., thick green curve vs. thick red curve in Fig. 7A, respectively). Knowing that: (i) all individuals of the same age had the same probability of losing primary vestibular afferents, MVN, MFs, and PFs; (ii) the degeneration process affected fibers and neurons based on random selection; (iii) the local and global homeostatic mechanisms (i.e., intrinsic plasticity and LTP and LTD) operated equally across all individuals, we reasoned that a possible determinant of VOR aging trajectory could lie in the distribution of the remaining fibers/synaptic connections post-age-related loss. We hypothesized that the activity of some subsets of the remaining connections might be more critical than others in terms of information content for the encoding of sensorimotor associations and then for maintaining VOR function. To test this hypothesis, we first sorted all individuals based on their VOR gain performance at 100 years. Then, we compared the subsets of residual connections active at specific VOR cycle moments across individuals. We found that the number of remaining connections responsible for the encoding of the peak and the trough of the eye velocity function correlated significantly with VOR performances of 100-year-old individuals (Fig. 7B and Supp. Fig. 5). That is, the sorting of 100-year-old individuals based on their residual VOR performance matched the sorting of the same individuals based on the number of residual PFs and MF–MVN projections that coded for the sinusoid's peak and trough. This correlation held already at 85 years of age (i.e., the cut off age between steady and declining VOR trajectories; Fig. 7B) and even at 60 years of age (i.e., numerous years before the discontinuity-time point between "good" and "bad" aging trajectories; Fig. 7B). Given that the overall number of lost connections was the same across all the study population, this implied that those individuals that

by chance had most of the remaining connections involved in the encoding of those two critical moments in the VOR period (i.e., between 200–300 ms and 700–800 ms) had the best chances to preserve their VOR performances throughout aging.

3. Discussion

This study presented a computational epidemiological model of cerebellum-dependent VOR adaptation. The proposed simulation framework attempted to provide a mechanistic insight into the factors that determine the impact of aging on rotatory VOR function. The model captured the neural computations at stake in the cerebellar circuit and it reproduced the biophysical properties of PCs. Importantly, the computational cross-sectional and longitudinal analyses presented in this work allowed the discrepancies among human VOR aging studies in the literature to be understood in terms of interindividual variability (in particular, in individuals over 80 years of age).

We tested the hypothesis that three neurosynaptic factors are key to relate age-related structural and functional VOR changes: the electrical coupling of IO neurons, LTP and LTD at PF–PC as well as MF–MVN synapses, and the intrinsic plasticity of PC synapses. To verify this hypothesis, we first ran a series of simulations to isolate the role of these three factors in determining VOR changes throughout aging. We found that vestibular structural losses caused by aging have consequences on the spatiotemporal activity patterns of the IO network. IO neural activity becomes simpler, similar to an on/off ensemble dynamic. This on/off network dynamic reduces the accuracy of retinal slip coding, which in turn impairs VOR adaptation. We tested the consequences on r-VOR aging by running a cross-sectional epidemiological simulation that isolated the effect of vestibular loss and IO coupling alteration, while blocking all compensatory mechanisms in the downstream cerebellar network. As expected, we found a linear decline of r-VOR gain as a function of age, determined by steady vestibular losses. This result contrasts with human epidemiological data, which show a well-preserved VOR function even in individuals aged 80 to 90 years (Li et al., 2015; Matiño-Soler et al., 2015; McGarvie et al., 2015).

Our second cross-sectional aging simulation indicated that LTP and LTD can sustain VOR function by enhancing the neural sensitivity to residual afferent signals throughout aging (i.e., it allowed the full synaptic range to be exploited in order to preserve the neuronal drives). However, the compensatory action by LTP and LTD became ineffective in the presence of significant levels of vestibular losses (i.e., beyond 85 years) because of synaptic weight saturation. This result is consistent with the hypothesis that a specific type of pre-training that desaturates synapses can improve the ability of mutant mice to learn an eye movement task (Nguyen-Vu et al., 2017). Conversely, Nguyen-Vu et al. (2017) found that a specific procedure that saturates synapses can impair the learning ability. In our model, the progressive saturation of PF–PC and MF–MVN synapses limited VOR adaptation, thus impairing the compensatory action of LTP and LTD in the oldest individual.

We then ran another cross-sectional simulation to assess the local homeostatic action of PCs' intrinsic plasticity, which adaptively increases PCs' neural excitability to signals transmitted by cerebellar granule cells. At the level of single PCs, we found that tonic firing rates increased with age, according to experimental data (Zhang et al., 2010), whereas the linear relation between the duration of post-complex spike pauses and the duration of pre-complex spike ISIs remained unchanged (testable prediction). At the level of VOR function, we found that intrinsic plasticity of PC synapses could moderately counter the vestibular structural losses, resulting in a slower, but still linear decline of
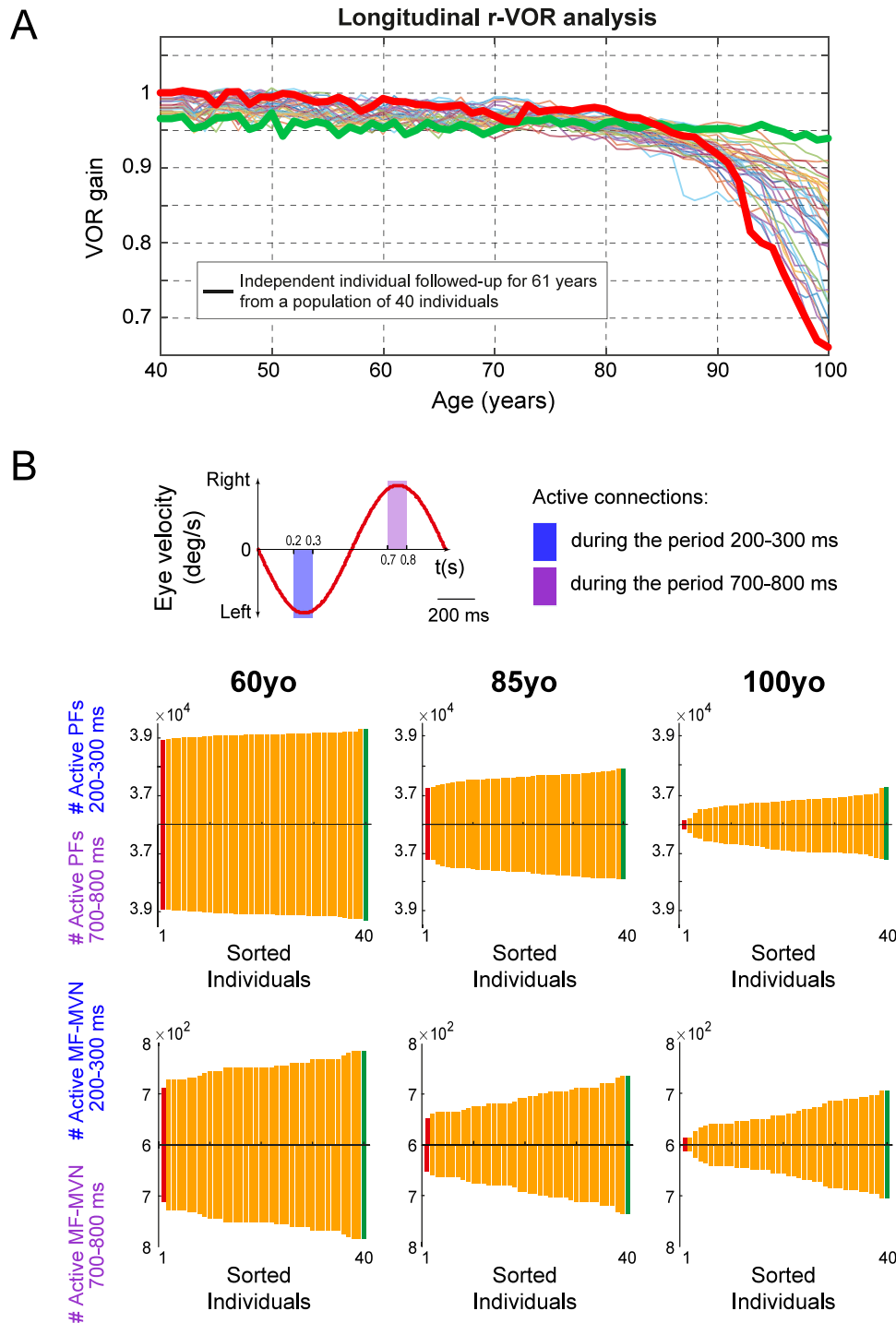
Fig. 7. Impact of aging on VOR: longitudinal study. (A) Longitudinal aging simulation accounting for vestibular loss, IO electrical coupling changes, PC intrinsic plasticity, and LTP/LTD at PF–PC and MF–MVN synapses. A study population of 40 individuals underwent a follow-up evaluation during 60 years (from 40 to 100 years of age), i.e., age-related changes accumulated longitudinally for each individual. The thick green and red curves correspond to the two individuals with best and worst VOR performance at 100 years of age, respectively. (B) Top: 1-Hz eye velocity function. The colored time windows correspond to the peak and the trough of the sinusoidal profile (i.e., between 200–300 ms and 700–800 ms). Residual PFs (center) and MF–MVN projections (bottom) active at the peak and the trough of the eye velocity profile across the study population. Individuals are sorted in ascending order on the basis of their VOR performance. The red and green individuals correspond to the worst and best 100-year-old individuals in A, respectively. Left column: distribution of residual PFs and MF–MVN connections at 60 yo. Central column: at 85 yo. Right column: at 100 yo. (For interpretation of the references to color in this figure legend, the reader is referred to the web version of this article.)

VOR accuracy over time. This result again contrasts with human epidemiological data.

We then ran a fourth cross-sectional simulation to assess how the three neuro-synaptic factors would work concurrently during

VOR aging. We found that the global homeostatic compensation mediated by cerebellar LTP and LTD was indeed primarily responsible for preserving VOR gain. The results also showed that the local homeostasis implemented by the intrinsic plasticity of PC synapses played a role in further sustaining VOR gain

in individuals 80–90 years old and in attenuating their decline afterwards. The slope attenuation was within the same range as the one recently reported in a study of PCs' intrinsic plasticity during long-term VOR consolidation in mice (Jang et al., 2020). In addition, the computational epidemiological results allowed us to evaluate the possible role of interindividual variability in biasing human VOR aging analyses, thus leading to discordant conclusions among previous studies in the literature (Smith, 2016). The model predicted that a sample size of 10 and 20 individuals per decade, as done in Matiño-Soler et al. (2015) and McGarvie et al. (2015), respectively, would led to very low probabilities of observing statistically significant VOR differences in those aged 70–79 versus those aged 80–89 (0.11 and 0.33, respectively). Accordingly, both Matiño-Soler et al. (2015) and McGarvie et al. (2015) reported a well-preserved VOR function across the life span (at least until 90 years of age). Our model also suggested that a sample size of 30 individual per decade, as used by Li et al. (2015), would lead to a probability of 0.63 of observing a VOR accuracy drop between the 70–79 and 80–89 age groups. Accordingly, and in contrast to other epidemiological studies, Li et al. (2015) reported some evidence for a decline of VOR function after 80–85 years of age.

Finally, we further exploited the presented computational epidemiology model to run a longitudinal aging simulation. This allowed us to follow individual aging trajectories over 60 years in an attempt to better understand the factors determining interindividual differences across aging (i.e., differentiating the steady and declining VOR trajectories). Importantly, we found that the number of remaining PFs and MF–MVN projections coding for the peak and the trough of the VOR cycle provided a predictive hallmark for the VOR aging trajectory on a single-subject basis. That is, individuals who lacked active PF and MF–MVN afferents in those precise moments were predicted to have more difficulties in VOR adaptation throughout aging. This prediction could be tested in animal models by seeking those fibers that are most active when the ocular velocity is maximal during VOR. For example, the identification of specific GCs (and of their PFs) that are active upon induction of specific stimulation is possible during in vivo mice experiments (Ishikawa et al., 2015).

The cerebellar model presented here made several assumptions. The first assumption was that the GC layer univocally encoded vestibular (related to head motion) signals through the temporal activation of non-overlapping cell populations during cerebellar VOR adaptation. GCs are thought to expand the coding space of vestibular signals (Carrillo et al., 2018) allowing interferences across tasks to be minimized and neuronal resources to be optimized (D'Angelo & De Zeeuw, 2009). The recurrent inhibitory Golgi cells − GC connections suggest the granular layer may act as a recurrent dynamic network (Yamazaki & Tanaka, 2005). Thus, GCs are likely to generate a randomly repetitive network response characterized by active/inactive state transitions with no repetition of active cell populations (Yamazaki & Tanaka, 2007). The model also assumed a progressive degradation of vestibular afferents integrated by the GC layer with aging (Baloh et al., 1989; Bergström, 1973), which led to a degradation of PFs, which in turn impaired long-term PF–PC synaptic adaptation. Notably, neural regeneration can occur at PF–PC synapses thanks to the Glu $\delta 2$ receptor (Ichikawa et al., 2016), whereas Glu $\delta 2$ deficits lead to disruption of LTD at PC synapses and motor impairment in VOR tasks (Pernice et al., 2019; Yuzaki, 2013). Some evidence has suggested that neural loss can be related to the absence of the Glu $\delta 2$ receptor, because the deletion of GluR $\delta 2$ expression in mutant mice (GluR $\delta 2$ho/ho) induces PC and GC reduction over a lifetime (Zanjani et al., 2016). A gradual decrease of Glu $\delta 2$ with aging would compromise Glu $\delta 2$-dependent processes that would then reduce intrinsic PC excitability and eventually impair LTD at PCs.

The model also assumed a compromised IO-IO electrical coupling due to degraded GABAergic afferents from MVN during aging. The strength of gap junctions among olivary neurons was modeled as asymmetric (De Zeeuw et al., 1998; Lefler et al., 2014). The level and the direction of this asymmetry were regulated by emulating the GABAergic feedback (Lefler et al., 2014). The coupling asymmetry allowed for the creation of different spatial configurations of PCs' complex spike patterns. The GABAergic inputs from MVN could directly cause a transient decrement in electrical coupling among IO cells (Lefler et al., 2014). GABAergic feedback not only temporarily blocked the transmission of signals through the olivary system but it also could isolate IO neurons from the network by shunting the junction current (Loewenstein, 2002). In the absence of GABAergic feedback, electrical coupling was not counteracted, and IO network oscillations were not mitigated but rather increased. There is only indirect evidence for an age-related degeneration of the GABAergic MVN inputs throughout aging. The r-aminobutyric acid, GABA, inhibits the formation of lipoxidation end products (Deng et al., 2010). The presence and accumulation of lipofuscin with aging, a lipoxidation product, are essential parts of the traditional theory of aging (Sulzer et al., 2008). Lipofuscin accumulates in postmitotic cells with age, impairing their functioning. Unbalanced cell metabolic and waste-degradation functions cause its presence. IO neurons are relatively immune to apoptosis (Lasn et al., 2001); they preserve their function with aging, although they tend to accumulate significant amount of lipofuscin with age (Brizzee et al., 1975). It is unclear whether the presence of a large amount of lipofuscin is a result of higher lipofuscin generation and/or decelerated removal (Fonseca et al., 2005). Because lipofuscin aggregates are unavoidable reactions in biological systems, the lack of a cycle involving lipofuscin elimination is more plausible than the absence of lipofuscin generation (Yin, 1996). The r-aminobutyric acid scavenging effects (Deng et al., 2010) over advanced lipoxidation end products (ALEs) may be instrumental in lipofuscin clearance in the olivary system. A gradual decline of r–aminobutyric acid presence with age may explain the accumulation of lipoxidation products in IO neurons. MVN GABAergic afferents are the main source of r-aminobutyric acid for the olivary cells, but they also mediate the electrical coupling among them. The gradual degeneration of these GABAergic afferents may explain the gradual presence of IO lipofuscin as well as the altered activations of IO ensembles with aging.

Limitations of the model

The cerebellar model separated MVN in 2 populations (inhibitory and excitatory, Fig. 1C). The excitatory population was meant to drive the motor neuron, whereas the inhibitory population (i.e., the MVN-IO afferents) was assumed to degrade with aging, so as the MVN-IO regulation of the IO–IO coupling. According to the olivo-cortico-nucleo-olivary (OCNO) model (Uusisaari & De Schutter, 2011), CFs originating from the same IO areas target PCs in the same narrow parasagittal bands in the cerebellar cortex. This band division is extended by the PC axons and IO collaterals into the cerebellar nuclei (MVN in the Flocculus), which target specific groups of nucleo-olivary (NO) neurons that project via MVN inhibitory neurons to the IO region belonging to the same loop (Fig. 1C).

Strict conservation of OCNO bands allows the cerebellar cortex to respond to olivary signals (complex spikes) in each cortical zone independently. During healthy aging, IO cells appear to be relatively immune to apoptosis (Escobar et al., 1968; Lasn et al., 2001; Moatamed, 1966; Monagle & Brody, 1974). In order for our cerebellar model to function, the neuron proportions of the OCNO loop had to be preserved. Indeed, the implemented retinal slip (error) coding by IO and cerebellar adaptation required the preservation of PC and MVN inhibitory type neurons to ensure

the independent operation of each modeled IO-PC–MVN-IO loop. Decreasing the number of MVN inhibitory neurons would require decreasing the number of neurons within the OCNO pathway accordingly (PC and IO), which would prevent the functioning of the implemented model. Hence, to maintain the anatomical integrity of the OCNO pathway, we simulated the consequences of healthy aging as a progressive degeneration of afferents and connections between neurons rather than neuronal losses.

4. Conclusion

This work addressed the link between structural and functional changes in VOR adaptation throughout aging. We proposed a computational model that posits three neurosynaptic factors that may synergistically determine VOR changes during aging: the electrical coupling between IO neurons; long-term spike-timing-dependent plasticity of PF–PC and MF–MVN synapses; and intrinsic plasticity of PC synapses.

By simulating cross-sectional and longitudinal evaluations across large scale study populations, we found that cerebellar long-term synaptic plasticity is likely to be responsible for the stable temporal profile of the aging VOR. Long-term plasticity would act as a global homeostatic mechanism that counters age-related vestibular neuroanatomical losses. We also found that the intrinsic plasticity of PCs may act as a local homeostatic mechanism, sustaining VOR at older ages. Importantly, our longitudinal aging simulations suggested that the efficacy of cerebellar local and global homeostatic compensation depends on the number of residual parallel and mossy fibers coding for the peak and the trough of the VOR cycle, which constitutes a predictive hallmark of the VOR aging trajectory on a single-subject basis. These testable predictions constitute a valuable insight into understanding the link between structural and functional aging of VOR and sensorimotor adaptation in general. To conclude, this work highlights the role of neurocomputational models in epidemiological research, and it contributes to cross-disciplinary research into human behavior.

5. Methods

5.1. Vestibulo-ocular reflex (VOR) model

The VOR was defined as a continuous-time mathematical model with two poles (Eq. (1)), whose parameters were adjusted recursively to fit experimental and clinical data (Gandhi et al., 2000; Gordon et al., 1989):

$$VOR(s) = \frac{E(s)}{H(s)} = \frac{K \cdot T_{c1} \cdot s}{(T_{c1} \cdot s + 1) \cdot (T_{c2} \cdot s + 1)} \cdot e^{-s\tau_{delay}} \quad (1)$$

where $e(t), \mathcal{L}\{e\}(s) = E(s) : eye\ motion(output)$, and $h(t), \mathcal{L}\{h\}(s) = H(s) : head\ motion\ (input)$

There were 4 parameters in the model: $Q = [K, T_{c1}, T_{c2}, \tau_{delay}]$. The delay parameter τ_{delay} captured the delay in communicating the signals from the inner ear to the brain and the eyes. This delay is the consequence of the time needed for neurotransmitters to traverse the synaptic clefts between nerve cells. Based on the number of synapses involved in the VOR, the estimate of this delay is of 5 ms (Robinson, 1981; Skavenski & Robinson, 1973). The gain parameter K, assumed to be between 0.6 and 1, modeled the fact that the eyes do not perfectly cope with the movement of the head (Robinson, 1981; Skavenski & Robinson, 1973). The T_{c1} parameter represented the dynamics associated with the semicircular canals as well as some additional neural processing. The canals are high-pass filters, as the neural active membranes in the canals slowly relax back to their resting position after rotational experimentation (the canals stop sensing

motion). Based on the mechanical characteristics of the canals, combined with additional neural processing which prolongs this time constant to improve the VOR accuracy, the T_{c1} parameter was estimated to be around 15 s, in agreement with the biologically range which is 10–30 s (Robinson, 1981; Skavenski & Robinson, 1973). Finally, the T_{c2} parameter captured the dynamics of the oculomotor plant, i.e. the eye and the muscles and tissues attached to it. Its value was between 0.005 and 0.05 s

To find the temporal response for the VOR transfer function, we needed to calculate the inverse Laplace transform (Eq. (2)). The outcome of the inverse Laplace transform consisted in a differential equation system defined in the same time domain as the spiking cerebellar network (see below; note that we modeled the delay and we inserted within the sensorimotor delay).

$$\begin{bmatrix} \dot{x}_1 \\ \dot{x}_2 \end{bmatrix} = \begin{bmatrix} 0 & 1 \\ -a_0 & -a_1 \end{bmatrix} \cdot \begin{bmatrix} x_1 \\ x_2 \end{bmatrix} + \begin{bmatrix} 0 \\ h(t) \end{bmatrix}$$

$$e(t) = \begin{bmatrix} b_0 & b_1 \end{bmatrix} \cdot \begin{bmatrix} x_1 \\ x_2 \end{bmatrix} \quad (2)$$

where:

$$a_0 = \frac{1}{T_{c1} \cdot T_{c2}}, \quad a_1 = \frac{T_{c1} + T_{c2}}{T_{c1} \cdot T_{c2}}$$

$$b_0 = 0, \quad b_1 = \frac{K \cdot T_{c1}}{T_{c1} \cdot T_{c2}}$$

VOR analysis and assessment. The periodic functions representing eye and head velocities were analyzed through a discrete-time Fourier transform:

$$FFT\ X(k) = \frac{1}{N} \sum_{n=0}^{N-1} x(n) \cdot e^{-j\frac{2 \cdot \pi \cdot k \cdot n}{N}}$$

$$Forward\ FFT\ x(n) = \frac{1}{N} \sum_{k=0}^{N-1} X(k) \cdot e^{j\frac{2 \cdot \pi \cdot k \cdot n}{N}} \quad (3)$$

where $x(n)$ indicates the periodic function, and N the number of samples within the considered time window. For each k, the term constituted a harmonic component (the complex version) with amplitude and frequency defined as:

$$Harmonic\ amplitude\ A_k = \frac{X(k)}{N}$$

$$Harmonic\ frequency\ f_k = \frac{F_s}{N} \quad (4)$$

with F_s denoting the sampling frequency (0.5 KHz). The harmonic distortion values, which indicated the harmonic content of a waveform compared to its fundamental, were negligible. We calculated the **VOR gain** as the ratio between the first harmonic amplitudes of the forward Fourier eye- and head-velocity transform.

$$VOR\ GAIN\ G = \frac{A_1^{eye-velocity}}{A_1^{head-velocity}} \quad (5)$$

VOR protocols. In rotational chair testing, the subject (mouse, monkey, human) is seated on a rotatory table (Dumas et al., 2016). Speed and velocity of rotation are controlled and measured. The subject's head is restrained, assuming that the movement of the table equals to the subject's head movement. During normal VOR adaptation, a visual target is given in anti-phase with vestibular stimulation. The eyes must follow the visual target thus minimizing the retinal slip. In the model, the eye output function was defined as:

$$Vestibular\ stimulation = \sin(2 \cdot \pi \cdot t)$$

$$Eye\ output\ function = A_E \cdot \sin(2 \cdot \pi \cdot t + \pi \cdot \phi_E) \quad (6)$$

where the ideal VOR experiment values corresponded to $A_E = -1, \phi_E = 0$ (visual field fixed).

5.2. Cerebellar network model

The cerebellar network model consisted of five neural populations (Fig. 1C).

Mossy fibers (MFs). 100 MFs constituted the input to the cerebellar network. Mossy fibers (MFs) conveyed the sensory signals from the vestibular organ and the eye muscles onto granule cells (GCs) and medial vestibular nuclei (MVN). MF activity evolved based on a sinusoidal function (1 Hz with a step size of 0.002 ms) to encode head movements consistently with the functional principles of VOR control (Arenz et al., 2008; Badura et al., 2016; Clopath et al., 2014; Lisberger & Fuchs, 1978). MF responses consisted of non-overlapping activations of equally sized neural subpopulations, which maintained a constant overall firing rate (Luque et al., 2016).

Granule cells (GCs). 2000 GCs operated as a state generator (Yamazaki & Tanaka, 2005, 2007, 2009). In the presence of a constant MF input, the granular layer generated a sequence of non-overlapping spatiotemporal patterns (i.e., states; Fujita, 1982). The same sequence of 500 states (each consisting of 4 active GCs per time step of 2 ms) repeatedly activated every 1-sec during learning (see below).

Purkinje cells (PCs). We modeled a population of 200 PCs, divided into 2 groups of 100 cells to control agonist and antagonist eye muscles, respectively. PCs integrated the excitatory input from the parallel fibers (PFs), i.e. the axons of GCs, as well as the input from the climbing fibers (CFs), i.e. the axons of inferior olive (IO) cells. PCs projected inhibitory connections onto MVN cells, to close the cerebellar loop and generate the VOR output.

Inferior olive (IO) and climbing fibers (CFs). We modeled 200 IO cells, divided in 2 groups of 100 IO cells for agonist / antagonist muscles, respectively. Each IO cell projected a CF onto one PC and one MVN cell. IO cells were interconnected via excitatory gap junctions, whose electrical coupling followed preferred directions (Devor & Yarom, 2002). The preferred paths were disposed radially from the center of 5×5 IO cell subpopulations, as in a square regular lattice network (Nobukawa & Nishimura, 2016). The strength of the electrical coupling, which drove the recurrent dynamics of the olivary population, was equal between all IO cells of the lattice network (see Table 1). In terms of external inputs, the IO population received excitatory afferents coding for retinal slips (Clopath et al., 2014). These inputs reached the center of each lattice network and they were generated by a Poisson spiking process (Boucheny et al., 2005; Luque et al., 2011b). The IO population also received an inhibitory external input from MVN cells (Fig. 1C) whose action regulated the IO network synchronization via electrical coupling modulation (Best & Regehr, 2009; Lefler et al., 2014). We assumed a progressive age-related decrease of this inhibitory action based on the progressive degeneration of MVN output (Torvik et al., 1986), which modulated the IO–IO synaptic weight distribution of each 5×5 IO cell subpopulation via the MVN-IO inhibitory action. The variance of the Gaussian IO–IO synaptic weight distribution varied linearly from 0.4 to 1.75 causing a more homogeneous electrical coupling along each 5×5 IO cell subpopulation whilst aging.

The error-related inputs (coding for retinal slips), combined with the recurrent electrical coupling modulated by inhibitory MVN inputs, determined the overall activity of the IO population, which generated the CF bursting output. The probabilistic spike sampling of retinal slips ensured an exploration of the whole error space over trials, whilst maintaining the CF activity below 10 Hz per fiber (in agreement with electrophysiological data Kuroda et al. (2001)). The evolution of the error could be sampled accurately even at such a low frequency (Carrillo et al., 2008;

Luque et al., 2011b). A graded representation of the error signal (Najafi & Medina, 2013) led to a correlation between the intensity of the sampled instantaneous error and the number of the spikes within the CF burst (Eq. (7)):

$$s_{spikes} : [0, 1] \subseteq R \rightarrow R$$

$$\varepsilon \rightarrow y = s_{spikes}(\varepsilon)$$

$$s_{spikes}(\varepsilon) = \begin{cases} 2 & if \quad 0.25 \leq \varepsilon \leq 0.50 \\ 3 & if \quad 0.50 \leq \varepsilon \leq 0.75 \\ 4 & if \quad 0.75 \leq \varepsilon \leq 0.85 \\ 5 & if \quad 0.85 \leq \varepsilon \leq 0.95 \\ 6 & if \quad 0.95 \leq \varepsilon \leq 1.0 \end{cases} \tag{7}$$

We assumed a perfect transmission of bursts from CFs to target PCs, i.e. the number of spikes in a PC complex spike linearly depended on the number of spikes in the CF burst (Mathy et al., 2009). The IO transmitted from 2 to 6 CF stimuli, delivered at inter-stimulus intervals of 2 ms, a range representative of inter-spike intervals recorded in olivary axons during bursts (Davie et al., 2008; Mathy et al., 2009), depending on the retinal slips to be compensated.

Medial Vestibular Nuclei (MVN) cells. We modeled a population of 200 MVN cells, with again 2 groups of 100 cells for agonist / antagonist muscles, respectively. Each MVN cell received an inhibitory afferent from a PC and an excitatory afferent from the IO cell that was also contacting that PC (Luque et al., 2014; Uusisaari & De Schutter, 2011). MVN cells also received excitatory projections from all MFs. The subcircuit IO-PC-MVN was then organized in a single microcomplex. This circuitry arrangement rested upon the principles of circuit integrity and uniformity on the olivo-cortico-nucleo-olivary (OCNO) loop (Uusisaari & De Schutter, 2011). The divergence–convergence ratios within the OCNO model, i.e., CFs to PC diverge onto 1:5-10, PC-CN 26:1 (Uusisaari & De Schutter, 2011), were simplified for the sake of computational tractability by modulating the synaptic weight strength accordingly (Table 1).

Translation of MVN spike trains into analog eye motor command. The MVN output was translated into analog output signals by averaging the spiking activity of each MVN subpopulation (one for each agonist / antagonist group of muscles) (Eqs. (8), (9)):

$$MVN_i(t) = \int_t^{t+T_{step}} \delta_{MVN_{spike}}(t) \cdot dt \tag{8}$$

$$MVN_{output}(t) = \alpha \left(\sum_{i=1}^{100} MVN_{ag,i}(t) - \sum_{j=1}^{100} MVN_{ant,j}(t) \right) \tag{9}$$

where α is the kernel amplitude that normalized the contribution of each MVN cell spike to the cerebellar output correction (the MVN_{ag} output controlled the agonist muscle, whilst the MVN_{ant} output controlled the antagonist muscle).

5.3. Neuronal models

MVN cell model. We modeled MVN cells as LIF neurons with excitatory (AMPA and NMDA) and inhibitory (GABA) chemical synapses (Eqs. (10)–(16)).

$$C_m \cdot \frac{dV}{dt} = I_{leaky} + I_{external} \tag{10}$$

$$I_{leaky} = g_L \cdot (E_L - V) \tag{11}$$

$$I_{external} = (g_{AMPA}(t) + g_{NMDA}(t) \cdot g_{NMDA\_INF}) \cdot (E_{AMPA} - V)$$

Table 1
Cerebellar network topology parameters.

Neurons		Synapses			
Pre-synaptic cells (number)	Post-synaptic cells (number)	Number	Type	Initial weight	Weight range
2000 GCs	200 PCs	400 000	AMPA	rand	[0, 3.65]
200 IO	200 PCs	200	AMPA	40	–
100 MFs	200 MVN	20 000	AMPA	0	[0, 1]
200 PCs	200 MVN	200	GABA	1.5	–
200 IO	200 MVN	200	NMDA	7	–
IO to IO (lattice configuration)		320	EC	5	–

Table 2
Neuronal model parameters.

Parameters	MVN	IO	GC
C_m (pF)	2	10	2
G_L (nS)	0.2	0.15	0.2
E_L (mV)	−70	−70	−70
E_{AMPA} (mV)	0	0	0
E_{GABA} (mV)	−80	−80	−80
τ_{AMPA} (ms)	0.5	1	0.5
τ_{NMDA} (ms)	14		
τ_{GABA} (ms)	10	2	10
V_{thr} (mV)	−40	−50	−40
T_{ref} (ms)	1	1.35	1
V_{peak} (mV)		31	

$$+ g_{GABA}(t) \cdot (E_{GABA} - V) \tag{12}$$

$$g_{AMPA}(t) = g_{AMPA}(t_0) \cdot e^{\frac{-(t-t_0)}{\tau_{AMPA}}} + \sum_{i=1}^{N} \delta_{AMPA,i}(t) \cdot w_i \tag{13}$$

$$g_{NMDA}(t) = g_{NMDA}(t_0) \cdot e^{\frac{-(t-t_0)}{\tau_{NMDA}}} + \sum_{i=1}^{N} \delta_{NMDA,i}(t) \cdot w_i \tag{14}$$

$$g_{GABA}(t) = g_{GABA}(t_0) \cdot e^{\frac{-(t-t_0)}{\tau_{GABA}}} + \sum_{i=1}^{N} \delta_{GABA,i}(t) \cdot w_i \tag{15}$$

$$g_{NMDA\_INF} = \frac{1}{1 + e^{-62 \cdot V} \cdot \frac{1.2}{3.57}} \tag{16}$$

where: C_m denoted de membrane capacitance; V the membrane potential; I_{leaky} the leak current; $I_{external}$ the external currents; E_L the resting potential; g_L the conductance responsible for the passive decay term toward the resting potential; w_i the synaptic weight of the synapses between the neuron i and the target neuron. Conductances $g_{AMPA}, g_{NMDA}, \ and \ g_{GABA}$ integrated all the contributions received by each receptor (AMPA, NMDA, and GABA) through individual synapses. These conductances were defined as decaying exponential functions, which were proportionally incremented via w_i upon each presynaptic spike arrival (Dirac delta function). Finally, g_{NMDA_INF} stood for the NMDA activation channel. Note that we set the neuron membrane potential to E_L during the refractory period (T_{ref}), just after reaching V_{thr} (voltage firing threshold) (Gerstner & Kistler, 2002; Gerstner et al., 2014). All the parameters of the point neuronal models are shown in Table 2.

Inferior olive (IO) neuronal model. We modeled IO cells as LIF neurons (Eqs. (10), (11)) with excitatory (AMPA, Eq. (13)) and inhibitory (GABA, Eq. (15)) chemical synapses as well as with electronic gap junctions (Llinas et al., 1974; Sotelo et al., 1974) (Eqs. (17), (18)):

$$I_{external} = g_{AMPA}(t) \cdot (E_{AMPA} - V) + g_{GABA}(t) \cdot (E_{GABA} - V) + I_{EC}$$

$$\tag{17}$$

$$I_{EC} = \sum_{i=1}^{N} w_i \cdot (V_i - V) \cdot \left(0.6 \cdot e^{-\frac{(V-V_i)^2}{50^2}} + 0.4 \right) \tag{18}$$

I_{EC} represented the total current injected through the electrical synapses (Schweighofer et al., 1999). V was the membrane potential of the target neuron, V_i the membrane potential of the neuron i, and N was the total number of input synapses of the target neuron. Finally, for a correct operation of the electrical synapses, this model emulated the depolarization and hyperpolarization phases of an action potential. The LIF neuron incorporated a simple threshold process that enabled the generation of a triangular voltage function (maximum/minimum value V_{peak}/E_L respectively) each time the neuron fired (Bezzi et al., 2004). All the parameters of the IO neuronal model are shown in Table 2.

Purkinje cell model. The PC model (Luque et al., 2019; Middleton et al., 2008; Miyasho et al., 2001) reproduced the three spiking modes of Purkinje cells, namely tonic, bursting, and spike pauses (Forrest, 2008). The PC model consisted of a single compartment with five ionic currents and two excitatory (AMPA, Eq. (13)) and inhibitory (GABA Eq. (15)) chemical synapses (Eqs. (19)–(21)):

$$C_m \cdot \frac{dV}{dt} = I_{internal} + I_{external} \tag{19}$$

$$I_{internal} = -g_K \cdot n^4 \cdot (V + 95) - g_{Na} \cdot m_0[V]^3 \cdot h \cdot (V - 50)$$

$$-g_{Ca} \cdot c^2 \cdot (V - 125) \tag{20}$$

$$-g_L \cdot (V + 70) - g_M \cdot M \cdot (V + 95)$$

$$I_{external} = g_{AMPA}(t) \cdot (E_{AMPA} - V) + g_{GABA}(t) \cdot (E_{GABA} - V) \tag{21}$$

where, g_K was the delayed rectifier potassium current, g_{Na} the transient inactivating sodium current, g_{Ca} the high-threshold non-inactivating calcium current, g_L the leak current, and g_M the muscarinic receptor suppressed potassium current (see Table 3).

The dynamics of each gating variable ($n, h, c,$ and M) followed Eq. (22):

$$\dot{x} = \frac{x_0[V] - x}{\tau_x[V]} \tag{22}$$

where x corresponds to variables $n, h, c,$ and M. The equilibrium function was given by the term $x_0[V]$ and the time constant $\tau_x[V]$ (see Table 3).

The sodium activation variable was replaced and approximated by its equilibrium function $m_0[V]$. The M current presented a temporal evolution significantly slower than the rest of variables. Each spike in the neuron generated a fast increase of the M current that took several milliseconds to return to its stable state. A high M current prevented the PC from entering in its tonic mode (when the neuron generated spikes due to PFs activity). A complex spike caused a rapid increase of the M current that depended, in turn, on the size of the spikelet within the burst. PC tonic mode resumed when the M current decreased.

We first validated the PC model in the NEURON simulator and then we reduced it to make it compatible with EDLUT (Luque et al., 2019). In the reduced PC model, we implemented the I_K and I_{Na} currents through a simple threshold process that triggered the

Table 3

PC, ionic conductance kinetic parameters. $g_k = 0.01$, $g_{Na} = 0.125$, $g_{Ca} = 0.001$, $g_m = 0.75$, $g_l = 0.2$ (mho/cm^2).

Conductance type	Steady-state Activation/Inactivation	Time constant (ms)
g_K delayed rectifier potassium current	$x_0[V] = \dfrac{1}{1 + e^{\frac{-V-29.5}{10}}}$	$\tau_x[V] = 0.25 + 4.35 \cdot e^{\frac{-|V+10|}{10}}$
g_{Na} transient inactivating sodium current	$x_0[V] = \dfrac{1}{1 + e^{\frac{V-59.4}{10.7}}}$	$\tau_x[V] = 0.15 + \dfrac{1.15}{1 + e^{\frac{V+33.5}{15}}}$
$m_0[V]$	$m_0[V] = \dfrac{1}{1 + e^{\frac{-V-48}{10}}} \cdot m$	

	Forward rate function (α)	Backward rate function (β)
g_{Ca} high threshold	$\alpha = \dfrac{1.6}{1 + e^{-0.0072 \cdot (V-5)}}$	$\beta = \dfrac{0.02 \cdot (V + 8.9)}{e^{\frac{V+8.9}{5}}}$
g_M muscarinic receptor suppressed potassium current	$\alpha = \dfrac{0.3}{1 + e^{\frac{-V-2}{5}}}$	$\beta = 0.001 \cdot e^{\frac{-V-70}{18}}$

	Steady–state Activation/Inactivation	Time constant (ms)
	$x_0[V] = \dfrac{\alpha}{\alpha + \beta}$	$\tau_x[V] = \dfrac{1}{\alpha + \beta}$

Table 4

PC, geometrical parameters.

Geometrical parameters	
Cylinder length of the soma	15 μm
Radius of the soma	8 μm
Membrane Capacitance	[1 - 0,64] μF/cm^2
Axial resistivity	100 Ω-cm (axon) 250 Ω-cm (dendrites)
Number of segments	1

generation of a triangular voltage function each time the neuron fired (Bezzi et al., 2004). This triangular voltage depolarization drove the state of ion channels similarly to the original voltage depolarization during the spike generation. The final internal current was given by Eq. (23):

$$I_{internal} = -g_{Ca} \cdot c^2 \cdot (V - 125) - g_L \cdot (V + 70) - g_M \cdot M \cdot (V + 95) \quad (23)$$

All the parameters are shown in Tables 3 and 4.

Mossy fibers (MF) & granule cells (GC) models. MFs were simulated merely as input neurons, i.e. parrot neurons, whereas GC neurons were simulated as LIF neurons (Eqs. (10), (11)), with the same excitatory (AMPA) and inhibitory (GABA) chemical synapses (Eqs. (13), (15)) and parameters contained in Table 2 (Luque et al., 2019).

5.4. Synaptic plasticity models

PC Intrinsic Plasticity. We equipped the PC model with a mechanism to update the value of the membrane capacitance (Cm) according to Eq. (24):

$$\frac{dC_m}{dt} = \frac{-\left(C_m - \frac{\beta}{2}\right)}{\beta \cdot \tau_{IP} \cdot (1 + I_{external})} \quad (24)$$

where τ_{IP} denoted the intrinsic plasticity time constant set to $12 \cdot 10^3$ s. This large time constant prevented interferences between intrinsic plasticity and other synaptic plasticity mechanisms during the learning process (Garrido et al., 2016). β controled the shape of the firing rate distribution and it was equal to 1 (see Garrido et al. (2016) for details about all intrinsic plasticity

mechanism parameters). Whenever a spike was elicited, the C_m variable was updated according to the following equation:

$$\Delta C_m = \frac{\varepsilon_{Cm}}{\tau_{IP}} \quad \text{if PC is active} \quad (25)$$

where $\varepsilon_{Cm} = 0.0475$ (Garrido et al., 2016) determined the influence of each spike on C_m. Note that the membrane capacitance of PCs could not diminish below a lower limit (0.77 ±0.17 μF/cm^2 where mean ± s.d.; range, 0.64–1.00 μF/cm^2, Roth and Häusser (2001).

PF–PC synaptic plasticity. The model of long-term depression (LTD) and long-term potentiation (LTP) at PF–PC synapses was the same as in Luque et al. (2019), and it followed Eqs. (26), (27):

$$LTD \; \Delta w_{PF_j - PC_i}(t) = \int_{-\infty}^{IO_{spike}} k\left(\frac{t - t_{IO_{spike}}}{\tau_{LTD}}\right) \cdot \delta_{GrC_{spike}}(t) \cdot dt$$
$$\text{if } PF_j \text{ is active at } t \quad (26)$$

$$LTP \; \Delta w_{PF_j - PC_i}(t) = \alpha \quad \text{if } PF_j \text{ is active at } t \quad (27)$$

where $\Delta w_{PF_j - PC_i}(t)$ denotes the weight change between the *j*th PF and the target *i*th PC; τ_{LTD} is the time constant that compensates for the sensory motor delay (Sargolzaei et al., 2016) (i.e., about 100 ms); δ_{GrC} is the Dirac delta function corresponding to an afferent spike from a PF; $\alpha = 0.023$; and the kernel function $k(x)$ is defined as in Eq. (28):

$$k(x) = e^{-x} \cdot \sin(x)^{20} \quad (28)$$

With this parametric configuration, the effect on presynaptic spikes arriving through PFs is maximal over the 100 ms time window before CF spike arrival, thus accounting for the sensorimotor pathway delay. For the sake of computational efficiency, note that the kernel $k(x)$ combines exponential and trigonometric functions that allow for recursive computation suitable for an event-driven simulation scheme as EDLUT (Naveros et al., 2017, 2015; Ros et al., 2006). Computational recursion avoids integrating the whole kernel upon each new spike arrival.

Finally, as shown in Eq. (27), the amount of LTP at PFs was fixed (Kawato & Gomi, 1992; Luque et al., 2011a, 2016), with an increase of synaptic efficacy equal to α each time a spike arrived through a PF to the targeted PC. This spike-timing-dependent plasticity (STDP) mechanism correlated the activity patterns coming through the PFs to PCs with the instructive signals coming from CFs to PCs (producing LTD in the activated PF–PC synapses). The correlation process at PC level identified certain PF activity patterns and it consequently reduced the PC output activity. A decrease of PC activations caused a subsequence reduction on the PC inhibitory action over the target MVN. Since the MVN received an almost constant gross MF activation, a lack of PC inhibitory action caused increasing levels of MVN activation. Conversely, the STDP mechanism increased the PC inhibitory activity by potentiating PF–PC synapses in the absence of instructive signal, thus causing decreasing levels of MVN activations. Consequently, PC axon activity governed MVN activation by shaping their inhibitory action produced onto MVN. This STDP mechanism, which regulated the LTP/LTD ratio at PF–PC synapses, shaped the inhibitory action of PCs onto MVN cells.

MF–MVN synaptic plasticity. The LTD/LTP dynamics at MF–MVN synapses were the same as in Luque et al. (2019), i.e., they were based on the following rules:

$$LTD \; \Delta w_{MF_j - MVN_i}(t) = \int_{-\infty}^{\infty} k\left(\frac{t - t_{PC_{spike}}}{\tau_{MF-MVN}}\right) \cdot \delta_{MF_{spike}}(t) \cdot dt$$
$$\text{if } MF_j \text{ is active at } t \quad (29)$$

$$LTP \; \Delta w_{MF_j - MVN_i}(t) = \alpha \quad \text{if } MF_j \text{ is active at } t \quad (30)$$

with $\Delta w_{MF_j - MVN_i}(t)$ denotes the weight change between the *jth* MF and the target *ith* MVN; $\tau_{MF-MVN} = 0.005$ the temporal width of the kernel; $\alpha = 0.00132$; and δ_{MF} the Dirac delta function that defined a MF spike. The integrative kernel function $k(x)$ was taken as:

$$k(x) = e^{-|x|} \cdot \cos(x)^2 \tag{31}$$

Note that there is no need for sensorimotor delay compensation thanks to the previous learning rule (τ_{LTD} in Eq. (26)). This second STDP mechanism accounted for learning consolidation at MVN (Luque et al., 2016). The PC output operated as an instructive signal and correlated the activity patterns coming from MFs to MVN (producing LTD in the activated MF–MVN synapses upon the arrival of the instructive signal and LTP otherwise). Well-timed sequences of increasing/decreasing levels of MVN activation ultimately shaped the cerebellar output during VOR adaptation.

The EDLUT source code is available at the following URL: www.ugr.es/~nluque/code_open/CODE_Cerebellar_Ageing_Vestibulo_Ocular_Adaptation.rar

CRediT authorship contribution statement

Niceto R. Luque: Conceived the initial idea, Designed set-up experimentation, Modeled and implemented the cerebellar network and the set-up experimentation, Prepared figures, Drafted the manuscript, Writing – review & editing. **Francisco Naveros:** Modeled and implemented the cerebellar network and the set-up experimentation, Writing – review & editing. **Denis Sheynikhovich:** Writing – review & editing. **Eduardo Ros:** Prepared figures, Drafted the manuscript, Writing – review & editing. **Angelo Arleo:** Conceived the initial idea, Designed set-up experimentation, Prepared figures, Drafted the manuscript, Writing – review & editing.

Declaration of competing interest

The authors declare that they have no known competing financial interests or personal relationships that could have appeared to influence the work reported in this paper.

Appendix A. Supplementary data

Supplementary material related to this article can be found online at https://doi.org/10.1016/j.neunet.2021.11.024.

References

Allen, D., Ribeiro, L., Arshad, Q., & Seemungal, B. M. (2017). Age-related vestibular loss: current understanding and future research directions. *Frontiers in Neurology, 7*, 231.

Alvarez, J. C., Dıaz, C., Suarez, C., Fernandez, J. A., Gonzalez del Rey, C., Navarro, A., & Tolivia, J. (2000). Aging and the human vestibular nuclei: morphometric analysis. *Mechanisms of Ageing and Development, 114*, 149–172.

Andersen, B. B., Gundersen, H. J. G., & Pakkenberg, B. (2003). Aging of the human cerebellum: a stereological study. *The Journal of Comparative Neurology, 466*, 356–365.

Anson, E., & Jeka, J. (2016). Perspectives on aging vestibular function. *Frontiers in Neurology, 6*, 269.

Arenz, A., Silver, R. A., Schaefer, A. T., & Margrie, T. W. (2008). The contribution of single synapses to sensory representation in vivo. *Science, 321*, 977–980.

Badura, A., Clopath, C., Schonewille, M., & De Zeeuw, C. I. (2016). Modeled changes of cerebellar activity in mutant mice are predictive of their learning impairments. *Scientific Reports, 6*, 36131.

Baloh, R. W., Jacobson, K. M., & Socotch, T. M. (1993). The effect of aging on visual-vestibuloocular responses. *Experimental Brain Research, 95*, 509–516.

Baloh, R. W., Sloane, P. D., & Honrubia, V. (1989). Quantitative vestibular function testing in elderly patients with dizziness. *Ear, Nose, & Throat Journal, 68*, 935–939.

Bergström, B. (1973). Morphology of the vestibular nerve: III. Analysis of the calibers of the myelinated vestibular nerve fibers in man at various ages. *ACTA Oto-laryngologica, 76*, 331–338.

Bertoni-Freddari, C., Fattoretti, P., Paoloni, R., Caselli, U., Galeazzi, L., & Meier-Ruge, W. (1996). Synaptic structural dynamics and aging. *Gerontology, 42*, 170–180.

Bertoni-Freddari, C., Giuli, C., Pieri, C., & Paci, D. (1986). Age-related morphological rearrangements of synaptic junctions in the rat cerebellum and hippocampus. *Archives of Gerontology and Geriatrics, 5*, 297–304.

Best, A. R., & Regehr, W. G. (2009). Inhibitory regulation of electrically coupled neurons in the inferior olive is mediated by asynchronous release of GABA. *Neuron, 62*, 555–565.

Bezzi, M., Nieus, T., Coenen, O. J.-M. D., & D'Angelo, E. (2004). An I & F model of a cerebellar granule cell. *Neurocomputing, 58*, 593–598.

Boucheny, C., Carrillo, R. R., Ros, E., & Coenen, O. J.-M. D. (2005). Real-time spiking neural network: an adaptive cerebellar model. *LNCS, 3512*, 136–144.

Brandt, T., Schautzer, F., Hamilton, D. A., Brüning, R., Markowitsch, H. J., Kalla, R., Darlington, C., Smith, P., & Strupp, M. (2005). Vestibular loss causes hippocampal atrophy and impaired spatial memory in humans. *Brain, 128*, 2732–2741.

Brizzee, K. R., Kaack, B., & Klara, P. (1975). Lipofuscin: intra-and extraneuronal accumulation and regional distribution. In *Neurobiology of aging* (pp. 463–484). Springer.

Carrillo, R. R., Naveros, F., Ros, E., & Luque, N. R. (2018). A metric for evaluating neural input representation in supervised learning networks. *Frontiers in Neuroscience, 12*.

Carrillo, R. R., Ros, E., Boucheny, C., & Coenen, O. (2008). A real-time spiking cerebellum model for learning robot control. *Biosystems, 94*, 18–27.

Chen, S., & Hillman, D. E. (1999). Dying-back of Purkinje cell dendrites with synapse loss in aging rats. *Journal of Neurocytology, 28*, 187–196.

Clopath, C., Badura, A., De Zeeuw, C. I., & Brunel, N. (2014). A cerebellar learning model of VOR adaptation in wild-type and mutant mice. *The Journal of Neuroscience, 34*, 7203–7215.

D'Angelo, E., & De Zeeuw, C. I. (2009). Timing and plasticity in the cerebellum: focus on the granular layer. *Trends in Neurosciences, 32*, 10.

D'Angelo, E., Mapelli, L., Casellato, C., Garrido, J. A., Luque, N. R., Monaco, J., Prestori, F., Pedrocchi, A., & Ros, E. (2016). Distributed circuit plasticity: new clues for the cerebellar mechanisms of learning. *Cerebellum, 15*, 139–151.

Davie, J. T., Clark, B. A., & Häusser, M. (2008). The origin of the complex spike in cerebellar Purkinje cells. *The Journal of Neuroscience, 28*, 7599–7609.

De Zeeuw, C. I., Hoogenraad, C. C., Koekkoek, S. K. E., Ruigrok, T. J., Galjart, N., & Simpson, J. I. (1998). Microcircuitry and function of the inferior olive. *Trends in Neurosciences, 21*, 391–400.

Demer, J. L., Honrubia, V., & Baloh, R. W. (1994). Dynamic visual acuity: a test for oscillopsia and vestibulo-ocular reflex function. *American Journal of Otolaryngology, 15*, 340–347.

Deng, Y., Xu, L., Zeng, X., Li, Z., Qin, B., & He, N. (2010). New perspective of GABA as an inhibitor of formation of advanced lipoxidation end-products: it's interaction with malondiadehyde. *Journal of Biomedical Nanotechnology, 6*, 318–324.

Desai, A., Goodman, V., Kapadia, N., Shay, B. L., & Szturm, T. (2010). Relationship between dynamic balance measures and functional performance in community-dwelling elderly people. *Physical Therapy, 90*, 748–760.

Devor, A., & Yarom, Y. (2002). Generation and propagation of subthreshold waves in a network of inferior olivary neurons. *Journal of Neurophysiology, 87*, 3059–3069.

Dits, J., Houben, M. M., & van der Steen, J. (2013). Three dimensional Vestibular ocular reflex testing using a Six degrees of freedom motion platform. *Journal of Visualized Experiments: JoVE*.

Dumas, G., Perrin, P., Ouedraogo, E., & Schmerber, S. (2016). How to perform the skull vibration-induced nystagmus test (SVINT). *European Annals of Oto-rhino-laryngology, Head & Neck Diseases, 133*, 343–348.

Escobar, A., Sampedro, E. D., & Dow, R. S. (1968). Quantitative data on the inferior olivary nucleus in man, cat and vampire bat. *The Journal of Comparative Neurology, 132*, 397–403.

Fonseca, D. B., Sheehy, M. R. J., Blackman, N., Shelton, P. M. J., & Prior, A. E. (2005). Reversal of a hallmark of brain ageing: lipofuscin accumulation. *Neurobiology of Aging, 26*, 69–76.

Forrest, M. (2008). *Biophysics of Purkinje computation*. University of Warwick.

Fujita, M. (1982). Adaptive filter model of the cerebellum. *Biological Cybernetics, 45*, 195–206.

Gandhi, C. C., Kelly, R. M., Wiley, R. G., & Walsh, T. J. (2000). Impaired acquisition of a Morris water maze task following selective destruction of cerebellar purkinje cells with OX7-saporin. *Behavioural Brain Research, 109*, 37–47.

Gao, Z., vanBeugen, B. J., & De Zeeuw, C. I. (2012). Distributed synergistic plasticity and cerebellar learning. *Nature Reviews Neuroscience, 13*, 1–17.

Garrido, J. A., Luque, N. R., Tolu, S., & D'Angelo, E. (2016). Oscillation-driven spike-timing dependent plasticity allows multiple overlapping pattern recognition in inhibitory interneuron networks. *International Journal of Neural Systems, 26*, Article 1650020.

Gerstner, W., & Kistler, W. M. (2002). *Spiking neuron models: Single neurons, populations, plasticity*. Cambridge University Press.

Gerstner, W., Kistler, W. M., Naud, R., & Paninski, L. (2014). *Neuronal dynamics: From single neurons to networks and models of cognition*. Cambridge University Press.

Gordon, J. L., Furman, J. M. R., & Kamen, E. W. (1989). System identification of the vestibulo-ocular reflex: application of the recursive least-squares algorithm. In *Bioengineering conference, 1989. Proceedings of the 1989 fifteenth annual Northeast* (pp. 199–200). IEEE.

Grasselli, G., He, Q., Wan, V., Adelman, J. P., Ohtsuki, G., & Hansel, C. (2016). Activity-dependent plasticity of spike pauses in cerebellar Purkinje cells. *Cell Reports, 14*, 2546–2553.

Grossman, G. E., & Leigh, R. J. (1990). Instability of gaze during locomotion in patients with deficient vestibular function. *Annals of Neurology, 27*, 528–532.

Ichikawa, R., Sakimura, K., & Watanabe, M. (2016). GluD2 endows parallel fiber–Purkinje cell synapses with a high regenerative capacity. *The Journal of Neuroscience, 36*, 4846–4858.

Ishikawa, T., Shimuta, M., & Häusser, M. (2015). Multimodal sensory integration in single cerebellar granule cells in vivo. *Elife, 4*, Article e12916.

Ito, M. (2013). Error detection and representation in the Olivo-Cerebellar system. *Frontiers in Neural Circuits, 1*, 1–8.

Jahn, K., Naezl, A., Schneider, E., Strupp, M., Brandt, T., & Dieterich, M. (2003). Inverse U-shaped curve for age dependency of torsional eye movement responses to galvanic vestibular stimulation. *Brain, 126*, 1579–1589.

Jang, D. C., Shim, H. G., & Kim, S. J. (2020). Intrinsic plasticity of cerebellar purkinje cells contributes to motor memory consolidation. *The Journal of Neuroscience, 40*, 4145–4157.

Kassardjian, C. D., Tan, Y. F., Chung, J. Y., Heskin, R., Peterson, M. J., & Broussard, D. M. (2005). The site of a motor memory shifts with consolidation. *The Journal of Neuroscience, 25*, 7979–7985.

Kawato, M., & Gomi, H. (1992). A computational model of four regions of the cerebellum based on feedback-error learning. *Biological Cybernetics, 68*, 95–103.

Kuroda, S., Yamamoto, K., Miyamoto, H., Doya, K., & Kawato, M. (2001). Statistical characteristics of climbing fiber spikes necessary for efficient cerebellar learning. *Biological Cybernetics, 84*, 183–192.

Lasn, H., Winblad, B., & Bogdanovic, N. (2001). The number of neurons in the inferior olivary nucleus in Alzheimer's disease and normal aging: A stereological study using the optical fractionator. *Journal of Alzheimer's Disease, 3*, 159–168.

Latorre, R., Aguirre, C., Rabinovich, M. I., & Varona, P. (2013). Transient dynamics and rhythm coordination of inferior olive spatio-temporal patterns. *Frontiers in Neural Circuits, 7*, 1–18.

Lefler, Y., Amsalem, O., Vrieler, N., Segev, I., & Yarom, Y. (2020). Using subthreshold events to characterize the functional architecture of the electrically coupled inferior olive network. *Elife, 9*, Article e43560.

Lefler, Y., Yarom, Y., & Uusisaari, M. Y. (2014). Cerebellar inhibitory input to the inferior olive decreases electrical coupling and blocks subthreshold oscillations. *Neuron, 81*, 1389–1400.

Leigh, R. J., & Zee, D. S. (2015). *The neurology of eye movements*. Oxford University Press.

Li, C., Layman, A. J., Geary, R., Anson, E., Carey, J. P., Ferrucci, L., & Agrawal, Y. (2015). Epidemiology of vestibulo-ocular reflex function: data from the Baltimore Longitudinal Study of Aging. *Otology & Neurotology, 36*, 267–272.

Lisberger, S. G., & Fuchs, A. F. (1978). Role of primate flocculus during rapid behavioral modification of VOR. II. Mossy fiber firing patterns during horizontal head rotation and eye movement. *Journal of Neurophysiology, 41*, 764–777.

Llinas, R., Baker, R., & Sotelo, C. (1974). Electrotonic coupling between neurons in cat inferior olive. *Journal of Neurophysiology, 37*, 560–571.

Loewenstein, Y. (2002). A possible role of olivary gap-junctions in the generation of physiological and pathological tremors. *Molecular Psychiatry, 7*, 129.

Lopez, I., Honrubia, V., & Baloh, R. W. (1996). Aging and the human vestibular nucleus. *Journal of Vestibular Research: Equilibrium & Orientation, 7*, 77–85.

Lorente de Nó, R. (1933). Vestibulo-ocular reflex arc. *Archives of Neurology & Psychiatry*.

Luque, N. R., Garrido, J. A., Carrillo, R. R., Coenen, O. J. M. D., & Ros, E. (2011a). Cerebellar input configuration toward object model abstraction in manipulation tasks. *IEEE Transactions on Neural Networks, 22*, 1321–1328.

Luque, N. R., Garrido, J. A., Carrillo, R. R., Coenen, O. J. M. D., & Ros, E. (2011b). Cerebellarlike corrective model inference engine for manipulation tasks. *IEEE Transactions on Systems, Man, and Cybernetics, 41*, 1299–1312.

Luque, N. R., Garrido, J. A., Carrillo, R. R., D'Angelo, E., & Ros, E. (2014). Fast convergence of learning requires plasticity between inferior olive and deep cerebellar nuclei in a manipulation task: a closed-loop robotic simulation. *Frontiers in Computational Neuroscience, 8*.

Luque, N. R., Garrido, J. A., Naveros, F., Carrillo, R. R., D'Angelo, E., & Ros, E. (2016). Distributed cerebellar motor learning; a STDP model. *Frontiers in Computational Neuroscience, 10*.

Luque, N. R., Naveros, F., Carrillo, R. R., Ros, E., & Arleo, A. (2019). Spike burst-pause dynamics of Purkinje cells regulate sensorimotor adaptation. *PLoS Computational Biology, 15*, Article e1006298.

Mathy, A., Ho, S. S., Davie, J. T., Duguid, I. C., Clark, B. A., & Hausser, M. (2009). Encoding of oscillations by axonal bursts in inferior olive neurons. *Neuron, 62*, 388–399.

Matiño-Soler, E., Esteller-More, E., Martin-Sanchez, J. C., Martinez-Sanchez, J. M., & Perez-Fernandez, N. (2015). Normative data on angular vestibulo-ocular responses in the yaw axis measured using the video head impulse test. *Otology & Neurotology, 36*, 466–471.

McGarvie, L. A., MacDougall, H. G., Halmagyi, G. M., Burgess, A. M., Weber, K. P., & Curthoys, I. S. (2015). The video head impulse test (vHIT) of semicircular canal function–age-dependent normative values of VOR gain in healthy subjects. *Frontiers in Neurology, 6*, 154.

Mergner, T., & Rosemeier, T. (1998). Interaction of vestibular, somatosensory and visual signals for postural control and motion perception under terrestrial and microgravity conditions—a conceptual model. *Brain Research Reviews, 28*, 118–135.

Middleton, S. J., Racca, C., Cunningham, M. O., Traub, R. D., Monyer, H., Knopfel, T., Schofield, I. S., Jenkins, A., & Whittington, M. A. (2008). High-frequency network oscillations in cerebellar cortex. *Neuron, 58*, 763–774.

Miyasho, T., Takagi, H., Suzuki, H., Watanabe, S., Inoue, M., Kudo, Y., & Miyakawa, H. (2001). Low-threshold potassium channels and a low-threshold calcium channel regulate Ca2+ spike firing in the dendrites of cerebellar Purkinje neurons: a modeling study. *Brain Research, 891*, 106–115.

Moatamed, F. (1966). Cell frequencies in the human inferior olivary nuclear complex. *Journal of Comparative Neurology, 128*, 109–116.

Monagle, R. D., & Brody, H. (1974). The effects of age upon the main nucleus of the inferior olive in the human. *The Journal of Comparative Neurology, 155*, 61–66.

Monteiro, R. A., Rocha, E., & Marini-Abreu, M. M. (1992). Age-related quantitative changes in inhibitory axo-somatic synapses on Purkinje cells of rat neocerebellum (Crus I and Crus II). *Journal of Submicroscopic Cytology & Pathology, 24*, 351–357.

Najac, M., & Raman, I. M. (2015). Integration of Purkinje cell inhibition by cerebellar nucleo-olivary neurons. *The Journal of Neuroscience, 35*, 544–549.

Najafi, F., & Medina, J. F. (2013). Beyond all-or-nothing climbing fibers: graded representation of teaching signals in Purkinje cells. *Frontiers in Neural Circuits, 7*, 1–15.

Naveros, F., Garrido, J. A., Carrillo, R. R., Ros, E., & Luque, N. R. (2017). Event-and time-driven techniques using parallel CPU–GPU co-processing for spiking neural networks. *Frontiers in Neuroinformatics, 11*.

Naveros, F., Luque, N. R., Garrido, J. A., Carrillo, R. R., Anguita, M., & Ros, E. (2015). A spiking neural simulator integrating event-driven and time-driven computation schemes using parallel CPU–GPU co-processing: A case study. *IEEE Transactions on Neural Networks and Learning Systems, 26*, 1567–1574.

Naveros, F., Luque, N. R., Ros, E., & Arleo, A. (2019). VOR adaptation on a humanoid icub robot using a spiking cerebellar model. *IEEE Transactions on Cybernetics*.

Nguyen-Vu, T. B., Zhao, G. Q., Lahiri, S., Kimpo, R. R., Lee, H., Ganguli, S., Shatz, C. J., & Raymond, J. L. (2017). A saturation hypothesis to explain both enhanced and impaired learning with enhanced plasticity. *Elife, 6*, Article e20147.

Nobukawa, S., & Nishimura, H. (2016). Chaotic resonance in coupled inferior olive neurons with the Llinás approach neuron model. *Neural Computation, 28*, 2505–2532.

Paige, G. D. (1992). Senescence of human visual-vestibular interactions. 1. Vestibulo-ocular reflex and adaptive plasticity with aging. *Journal of Vestibular Research: Equilibrium & Orientation, 2*, 133–151.

Palay, S. L., & Chan-Palay, V. (2012). *Cerebellar cortex: Cytology and organization.* Springer Science & Business Media.

Pernice, H. F., Schieweck, R., Jafari, M., Straub, T., Bilban, M., Kiebler, M. A., & Popper, B. (2019). Altered glutamate receptor Ionotropic Delta subunit 2 expression in Stau2-deficient cerebellar Purkinje cells in the adult brain. *International Journal of Molecular Sciences, 20*, 1797.

Peterka, R. J., Black, F. O., & Schoenhoff, M. B. (1990). Age-related changes in human vestibulo-ocular reflexes: sinusoidal rotation and caloric tests. *Journal of Vestibular Research, 1*, 49–59.

Piirtola, M., & Era, P. (2006). Force platform measurements as predictors of falls among older people–a review. *Gerontology, 52*, 1–16.

Renovell, A., Giner, J., & Portoles, M. (2001). Loss of granule neurons in the aging human cerebellar cortex. *The International Journal of Developmental Biology, 40*, S193–S194.

Robinson, D. A. (1981). The use of control systems analysis in the neurophysiology of eye movements. *Annual Review of Neuroscience, 4*, 463–503.

Ros, E., Carrillo, R. R., Ortigosa, E. M., Barbour, B., & Agís, R. (2006). Event-driven simulation scheme for spiking neural networks using lookup tables to characterize neuronal dynamics. *Neural Computation, 18*, 2959–2993.

Roth, A., & Häusser, M. (2001). Compartmental models of rat cerebellar purkinje cells based on simultaneous somatic and dendritic patch-clamp recordings. *Journal Physiology, 535*, 445–472.

Santina, C. C., Cremer, P. D., Carey, J. P., & Minor, L. B. (2001). The vestibulo-ocular reflex during self-generated head movements by human subjects with unilateral vestibular hypofunction. *Annals New York Academy of Sciences, 942*, 465–466.

Sargolzaei, A., Abdelghani, M., Yen, K. K., & Sargolzaei, S. (2016). Sensorimotor control: computing the immediate future from the delayed present. *BMC Bioinformatics, 17*, 501–509.

Schweighofer, N., Doya, K., & Kawato, M. (1999). Electrophysiological properties of inferior olive neurons: a compartmental model. *Journal of Neurophysiology, 82*, 804–817.

Shim, H. G., Lee, Y.-S., & Kim, S. J. (2018). The emerging concept of intrinsic plasticity: activity-dependent modulation of intrinsic excitability in cerebellar Purkinje cells and motor learning. *Experimental Neurobiology, 27*, 139.

Shutoh, F., Ohki, M., Kitazawa, H., Itohara, S., & Nagao, S. (2006). Memory trace of motor learning shifts transsynaptically from cerebellar cortex to nuclei for consolidation. *Neuroscience, 139*, 767–777.

Skavenski, A. A., & Robinson, D. A. (1973). Role of abducens neurons in vestibuloocular reflex. *Journal of Neurophysiology, 36*, 724–738.

Smith, P. F. (2016). Age-related neurochemical changes in the vestibular nuclei. *Frontiers in Neurology, 7*, 20.

Sotelo, C., Llinas, R., & Baker, R. (1974). Structural study of inferior olivary nucleus of the cat: morphological correlates of electrotonic coupling. *Journal of Neurophysiology, 37*, 541–559.

Sulzer, D., Mosharov, E., Talloczy, Z., Zucca, F. A., Simon, J. D., & Zecca, L. (2008). Neuronal pigmented autophagic vacuoles: lipofuscin, neuromelanin, and ceroid as macroautophagic responses during aging and disease. *Journal of Neurochemistry, 106*, 24–36.

Tinetti, M. E. (2003). Preventing falls in elderly persons. *The New England Journal of Medicine, 348*, 42–49.

Torvik, A., Torp, S., & Lindboe, C. F. (1986). Atrophy of the cerebellar vermis in ageing: a morphometric and histologic study. *Journal of the Neurological Sciences, 76*, 283–294.

Uusisaari, M., & De Schutter, E. (2011). The mysterious microcircuitry of the cerebellar nuclei. *Journal Physiology, 589*, 3441–3457.

Viswasom, A. A., Sivan, S., & Jobby, A. (2013). Age related changes in the granule cell number in the human cerebellar cortex. *Journal of Evolution of Medical and Dental Sciences, 2*, 2698–2705.

Yamazaki, T., & Tanaka, S. (2005). Neural modeling of an internal clock. *Neural Computation, 17*, 1032–1058.

Yamazaki, T., & Tanaka, S. (2007). The cerebellum as a liquid state machine. *Neural Networks, 20*, 290–297.

Yamazaki, T., & Tanaka, S. (2009). Computational models of timing mechanisms in the cerebellar granular layer. *Cerebellum, 8*, 423–432.

Yin, D. (1996). Biochemical basis of lipofuscin, ceroid, and age pigment-like fluorophores. *Free Radical Biology and Medicine, 21*, 871–888.

Yuzaki, M. (2013). Cerebellar LTD vs. motor learning—lessons learned from studying GluD2. *Neural Networks, 47*, 36–41.

Zalewski, C. K. (2015). Aging of the human vestibular system. In *Seminars in hearing, Vol. 36* (pp. 175–196). Thieme Medical Publishers.

Zanjani, H. S., Vogel, M. W., & Mariani, J. (2016). Deletion of the GluR δ2 receptor in the hotfoot mouse mutant causes granule cell loss, delayed Purkinje cell death, and reductions in purkinje cell dendritic tree area. *Cerebellum, 15*, 755–766.

Zhang, C., Zhu, Q., & Hua, T. (2010). Aging of cerebellar Purkinje cells. *Cell and Tissue Research, 341*, 341–347.